Advances in Engineering Software 160 (2021) 102962

Contents lists available at ScienceDirect

Advances in Engineering Software

journal homepage: www.elsevier.com/locate/advengsoft

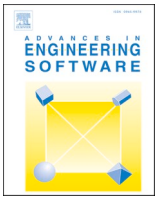

Asynchronous distributed-memory task-parallel algorithm for compressible flows on unstructured 3D Eulerian grids

J. Bakosi [*,a], R. Bird [a], F. Gonzalez [c], C. Junghans [a], W. Li [b], H. Luo [b], A. Pandare [a], J. Waltz [a]

[a] Los Alamos National Laboratory, Los Alamos, NM, United States
[b] North Carolina State University, Raleigh, NC, United States
[c] Strong Analytics, Chicago, IL, United States

ARTICLE INFO

Keywords:
Shock hydrodynamics
Finite element method
Flux-corrected transport
Charm++
Automatic load balancing

ABSTRACT

We discuss the implementation of a finite element method, used to numerically solve the Euler equations of compressible flows, using an asynchronous runtime system (RTS). The algorithm is implemented for distributed-memory machines, using stationary unstructured 3D meshes, combining data-, and task-parallelism on top of the Charm++ RTS. Charm++'s execution model is asynchronous by default, allowing arbitrary overlap of computation and communication. Task-parallelism allows scheduling parts of an algorithm independently of, or dependent on, each other. Built-in automatic load balancing enables continuous redistribution of computational load by migration of work units based on real-time CPU load measurement. The RTS also features automatic checkpointing, fault tolerance, resilience against hardware failure, and supports power-, and energy-aware computation. We demonstrate scalability up to 25×10^9 cells at $\mathcal{O}(10^4)$ compute cores and the benefits of automatic load balancing for irregular workloads. The full source code with documentation is available at https://quinoacomputing.org.

1. Introduction

The numerical solution of the governing equations of fluids has a long history. The most popular methods to solve the Euler equations, governing inviscid flows, use finite difference (FD) [1], finite volume (FV) [2], and more recently, finite element (FE) methods [3]. While historically FD methods were developed first, today all of FD, FV, and FE methods enjoy wide popularity due to their respective strengths, depending on the type and needs of their application (e.g., complex flow geometries), algorithmic requirements (e.g., direct numerical simulation of turbulence), and suitability for various supercomputing hardware (e.g., graphics processing units).

This paper describes the software implementation of a numerical method, suitable to solve the single-fluid Euler equations in complex 3D geometries, governing high-speed compressible flows, as required, e.g., in aerodynamics applications. The numerical method belongs to the FE family, developed in the 1980s, still useful today, due to its simplicity and low computational cost. The main contribution of this paper is to provide an example of how such a method can be implemented using an asynchronous, distributed-memory runtime system, that enables good parallel scalability to large computers ($> 10^4$ CPUs), required for large problems ($> 10^7$ mesh cells). Compard to synchronous programming, resulting in frequent but often unnecessary syncrhonization points imposed by the programming paradigm, asynchronous programming enables more overlap of computation, communication, and I/O. In addition, using the Charm++ runtime system (instead of the more common message passing paradigm, MPI) allows automatic load balancing, without requiring code from the application developer, independent of the source of the parallel load-imbalance, due to, e.g., adaptive mesh refinement, costlier local equations of state, higher order polynomials, etc.

2. Objective

This paper discusses the numerical implementation, verification, and performance of a finite element method for compressible high-speed flows for 3D unstructured grids using the Charm++ runtime system. The numerical method discussed closely follows [4] and we make no claims on its numerical accuracy, other than verifying its correctness, its design order of convergence for smooth solutions, and its convergence for discontinuous solutions. The main contribution is the discussion of the software implementation on Charm++ using an asynchronous

* Corresponding author.
E-mail address: jbakosi@lanl.gov (J. Bakosi).

https://doi.org/10.1016/j.advengsoft.2020.102962
Received 8 June 2020; Received in revised form 14 October 2020; Accepted 24 December 2020
Available online 6 July 2021

parallel computing paradigm targeting both shared-, and distributed-memory architectures. The main benefits of Charm++ are to allow arbitrary overlap of computation and communication, automatic checkpoint/restart, automatic fault tolerance, and automatic load balancing based on real-time CPU load measurement that is independent of the algorithm, leading to separation of concerns, code modularity, usability, and significantly increased performance. These features make such an implementation especially suitable for large multiphysics simulations with a priori unknown, heterogeneous, and/or dynamic parallel load distribution.

The structure of the paper is as follows. In Section 3 we present the governing equations solved. Section 4 describes the numerical method. Section 5 gives a brief overview of the Charm++ runtime system, discussing the features used by the flow solver, and gives some details on the high level software design, and algorithmic choices. Section 6 discusses a set of test problems used for solution and implementation verification. Section 7 discusses scalability, parallel performance, and load balancing. Finally, Section 8 contains a summary and conclusions.

3. The equations of compressible flow

The governing equations under consideration are the 3D unsteady Euler equations, governing inviscid compressible flow, written here in flux-conservative form

$$\frac{\partial U}{\partial t}+\frac{\partial F_j}{\partial x_j}=S, \qquad U=\begin{Bmatrix}\rho\\ \rho u_i\\ \rho E\end{Bmatrix}, F_j=\begin{Bmatrix}\rho u_j\\ \rho u_i u_j+p\delta_{ij}\\ u_j(\rho E+p)\end{Bmatrix}, S=\begin{Bmatrix}S_\rho\\ S_{u,i}\\ S_E\end{Bmatrix}, \tag{1}$$

where the summation convention on repeated indices has been applied, and ρ is the density, u_i the velocity vector, $E=u_iu_i/2+e$ is the specific total energy, e is the specific internal energy, and p is the pressure. S_ρ, $S_{u,i}$, and S_E are source terms that arise from the application of the method of manufactured solutions, used for verification; these source terms are zero when computing practical engineering problems. The system is closed with the ideal gas law equation of state

$$p=\rho e(\gamma-1), \tag{2}$$

where γ is the ratio of specific heats. The exact form of the equation of state is of secondary importance for this work, in principle any analytic or tabular equation of state could be used.

4. The flow solver

This section describes discretization in space (Section 4.1) and time (Section 4.2), and flux-corrected transport (Section 4.3). The method is based on a continuous Galerkin finite element method for linear tetrahedra.

4.1. Discretization in space

To arrive at a continuous Galerkin finite element method we start from the weak form of the governing Eq. (1),

$$\int_\Omega N^v\left(\frac{\partial U}{\partial t}+\frac{\partial F_j}{\partial x_j}-S\right)\mathrm{d}\Omega=0, \quad v=1,2,\ldots,n, \tag{3}$$

which requires that the error in the numerical solution, sampled at n discrete points, v, using the weighting functions N^v, vanish on the whole domain, Ω, in an integral sense. Numerically approximating the solution as $U\approx N^w\widehat{U}_w$, where $\widehat{U}_w$ denotes the unknowns at the discrete node w, leads to the Galerkin weak statement

$$\int_\Omega N^v\left[N^w\frac{\partial\widehat{U}_w}{\partial t}+\frac{\partial}{\partial x_j}F_j\left(N^w\widehat{U}_w\right)-S\left(N^w\widehat{U}_w\right)\right]\mathrm{d}\Omega=0. \tag{4}$$

Integrating the flux term by parts, neglecting the resulting boundary> integral (assuming zero flux on the problem boundary), and applying $F_j(N^w\widehat{U}_w)\approx N^wF_j(\widehat{U}_w)$ and $S(N^w\widehat{U}_w)\approx N^wS(\widehat{U}_w)$ see [3], yields the final weak form for the whole domain, Ω,

$$\int_\Omega N^vN^w\mathrm{d}\Omega\frac{\partial\widehat{U}_w}{\partial t}-\int_\Omega N^w\mathrm{d}\Omega\frac{\partial N^v}{\partial x_j}F_j\left(\widehat{U}_w\right)-\int_\Omega N^vN^w\mathrm{d}\Omega S\left(\widehat{U}_w\right)=0. \tag{5}$$

All integrals in Eq. (5) are evaluated by breaking up the domain, Ω, into sub-domains as a sum over integrals over discrete elements, Ω_e,

$$\sum_{\Omega_e}\sum_{v\in\Omega_e}\int_{\Omega_e}N^vN^w\mathrm{d}\Omega_e\frac{\partial\widehat{U}_w}{\partial t}=\sum_{\Omega_e}\sum_{v\in\Omega_e}\int_{\Omega_e}N^w\mathrm{d}\Omega_e\frac{\partial N^v}{\partial x_j}F_j\left(\widehat{U}_w\right)+\sum_{\Omega_e}\sum_{v\in\Omega_e}\int_{\Omega}N^vN^w\mathrm{d}\Omega S\left(\widehat{U}_w\right), \tag{6}$$

where the inner summation is over points w forming Ω_e (gather) and the outer summation is over tetrahedra Ω_e connected to point v (scatter). Eq. (6) results in the following semi-discrete system of equations

$$\mathbf{M}_c\widehat{\mathbf{U}}_{,t}=\mathbf{r}\left(\widehat{\mathbf{U}}\right), \tag{7}$$

where the comma denotes a derivative. The size of the consistent mass matrix M_c is $n\times n$, where n is the number of nodes of the computational mesh. According to the sum in Eq. (6), only those elements contribute to a given row v of $\mathbf{M}_c$ which contain node v (scatter), thus $\mathbf{M}_c$ is sparse.

4.2. Discretization in time

Eq. (7) is discretized in time using a Lax–Wendroff (Taylor–Galerkin) scheme [5–7] implemented using two stages:

$$\begin{aligned}U^{n+1/2} &= U^n+\frac{\Delta t}{2}U^n_{,t}=U^n-\frac{\Delta t}{2}\frac{\partial}{\partial x_j}F_j(U^n)+\frac{\Delta t}{2}S(U^n),\\ \Delta U &= U^{n+1}-U^n=\Delta tU^{n+1/2}_{,t}=-\Delta t\frac{\partial}{\partial x_j}F_j\left(U^{n+1/2}\right)+\Delta tS\left(U^{n+1/2}\right).\end{aligned} \tag{8}$$

The above scheme combined with linear shape functions is identical to a two-stage Runge–Kutta Galerkin finite element method, and thus central differencing without damping. Stabilization is obtained by using constant shape functions for the half step solution where the gather results in element quantities, followed by a scatter step using linear shape functions resulting in nodal quantities. Assuming linear tetrahedra, the combined spatial and temporal discretization that achieves this yields the following staggered scheme [3],

$$\begin{aligned}U^{n+1/2}_e&=\frac{1}{4}\sum_{w=1}^4\widehat{U}^n_w-\frac{\Delta t}{2}\sum_{w=1}^4\frac{\partial N^w}{\partial x_j}F_j\left(\widehat{U}^n_w\right)+\frac{\Delta t}{2}\frac{1}{4}\sum_{w=1}^4S\left(\widehat{U}^n_w\right),\\ \sum_{\Omega_e}\sum_{v\in\Omega_e}\int_{\Omega_e}N^vN^w\mathrm{d}\Omega_e\Delta\widehat{U}_w&=\Delta t\int_{\Omega_e}\frac{\partial N^v}{\partial x_j}F_j\left(U^{n+1/2}_e\right)\mathrm{d}\Omega_e+\Delta t\int_{\Omega_e}N^vS\left(U^{n+1/2}_e\right)\mathrm{d}\Omega_e\end{aligned} \tag{9}$$

where $U^{n+1/2}_e$ is the vector of element-centered solutions at the half step. Note that the first step discretizes the flux integral *before* integration by parts, Eq. (4), while the second one *after* integration by parts, Eq. (5),

hence the difference in sign.

4.3. Flux-corrected transport

Flux-corrected transport (FCT) is a solution to circumvent the consequence of Godunov's theorem [8], which states that no linear scheme of order greater than 1 will yield monotonic solutions. Accordingly, FCT is a nonlinear scheme that combines a high-, and a low-order scheme using limiting.

In the FCT scheme we use, the high-order solution at the new time step can be written as

$$\mathbf{U}^{n+1} = \mathbf{U}^n + \Delta\mathbf{U}^h = \mathbf{U}^n + \Delta\mathbf{U}^l + \left(\Delta\mathbf{U}^h - \Delta\mathbf{U}^l\right) = \mathbf{U}^l + \left(\Delta\mathbf{U}^h - \Delta\mathbf{U}^l\right), \tag{10}$$

where $\Delta\mathbf{U}^h$ and $\Delta\mathbf{U}^l$ denote the solution increments of the high-, and low-order schemes, respectively. In Eq. (10), it is the last term that is limited in a way to avoid spurious oscillations as

$$\mathbf{U}^{n+1} = \mathbf{U}^l + \lim\left(\Delta\mathbf{U}^h - \Delta\mathbf{U}^l\right). \tag{11}$$

The high-order scheme scheme, given in Eq. (9), is symbolically written as

$$\mathbf{M}_c\Delta\mathbf{U}^h = \mathbf{r}. \tag{12}$$

From Eq. (12) we construct a low order scheme by lumping the mass matrix and adding mass diffusion

$$\mathbf{M}_l\Delta\mathbf{U}^l = \mathbf{r} + \mathbf{d} = \mathbf{r} - c_\tau(\mathbf{M}_l - \mathbf{M}_c)\mathbf{U} \tag{13}$$

where $\mathbf{M}_l$ is the lumped mass matrix and c_τ is a diffusion coefficient. Using $c_\tau = 1$ guarantees a monotone low order solution, [3]. If we rewrite Eq. (12) as

$$\mathbf{M}_l\Delta\mathbf{U}^h = \mathbf{r} + (\mathbf{M}_l - \mathbf{M}_c)\Delta\mathbf{U}^h, \tag{14}$$

the difference between the right hand sides of the high and low order schemes can be recognized as

$$\mathrm{AEC} = \Delta\mathbf{U}^h - \Delta\mathbf{U}^l = \mathbf{M}_l^{-1}(\mathbf{M}_l - \mathbf{M}_c)\left(c_\tau\mathbf{U}^n + \Delta\mathbf{U}^h\right), \tag{15}$$

also called as the anti-diffusive element contributions (AEC). The AEC is then limited, $C_e\cdot\mathrm{AEC}$, and applied to advance the solution to the next time step using Eq. (11), where $0 \le C_e \le 1$ is the limit coefficient for a given element e.

4.4. The limiting procedure

The limiting procedure to compute C_e closely follows [4]. The description here is given in terms of how the algorithm is broken up into computational tasks to prepare for the discussion on task-parallelism later.

Task Left-hand side **(LHS)**

Eq. (6) shows that the LHS is the consistent mass matrix. $\mathbf{M}_c$ is lumped by summing the rows to the diagonals. Inverting $\mathbf{M}_c$ distributed across computers would be costly. Using a lumped (diagonal) matrix instead reduces computational cost and software complexity at the cost of some additional numerical error but does not reduce the order of accuracy of the method [3]. If the mesh does not move and its topology does not change, the LHS needs no update between time steps.

Task Right-hand side **(RHS)**

The high-order right hand side is computed by the two-step procedure given by Eq. (9). Since the two steps are staggered, the gather takes information from nodes to cell centers, followed by a scatter, moving information from cells to nodes, both steps are contained within a single right hand side calculation within a time step. Within the two steps there is no need for parallel communication as an element always resides on a given mesh partition and only mesh nodes are shared between processing elements (PEs), whose solution values are communicated.

Task Diffusion **(DIF)**

A step of the limiting procedure is to compute the mass diffusion term in Eq. (13). Using linear tetrahedra, this is given for each element by

$$-[c_\tau(\mathbf{M}_l - \mathbf{M}_c)]_e = -\frac{c_\tau J_e}{120}\begin{bmatrix} -3 & -1 & -1 & -1 \\ -1 & -3 & -1 & -1 \\ -1 & -1 & -3 & -1 \\ -1 & -1 & -1 & -3 \end{bmatrix}, \tag{16}$$

where $J_e = \overrightarrow{BA}\cdot(\overrightarrow{CA}\times\overrightarrow{DA})$ is the element Jacobian, computed from the triple product of the edge vectors of the tetrahedron given by vertices A, B, C, and D.

Task Anti-diffusive element contributions **(AEC)**

Another step is to compute the anti-diffusive element contributions, given in Eq. (15), for each element. For this $\mathbf{M}_l - \mathbf{M}_c$ is given in Eq. (16), and the inverse of the lumped mass matrix, $\mathbf{M}_l^{-1}$ is obtained from the nodal cell volumes, computed by summing the quarter of each tetrahedron element volume to nodes. Once the AECs are computed for each element, the next immediate step is to sum all positive (negative) anti-diffusive element contributions to node i

$$P_i^\pm = \sum_e \left\{ \begin{matrix} \max \\ \min \end{matrix} \right\}(0, \mathrm{AEC}_e). \tag{17}$$

Task Allowed limits **(ALW)**

The limiting procedure requires the maximum and minimum nodal values of the low-order solution, $\mathbf{U}^l$, and the previous solution, $\mathbf{U}^n$,

$$\mathbf{U}_i^* = \left\{ \begin{matrix} \max \\ \min \end{matrix} \right\}\left(\mathbf{U}_i^l, \mathbf{U}^n\right). \tag{18}$$

Another alternative is to only consider the low order solution, $\mathbf{U}_l$, when computing the allowed solution bounds, which leads to the so-called 'clipping limiter' in place of Eq. (18): $\mathbf{U}_i^* = \mathbf{U}_i^l$. This is followed by computing the maximum and minimum nodal values of all elements,

$$\mathbf{U}_e^* = \left\{ \begin{matrix} \max \\ \min \end{matrix} \right\}\left(\mathbf{U}_A^*, \mathbf{U}_B^*, \mathbf{U}_C^*, \mathbf{U}_D^*\right), \tag{19}$$

then computing the maximum and minimum unknowns of the elements surrounding each node,

$$\mathbf{U}_i^{\begin{matrix} \max \\ \min \end{matrix}} = \left\{ \begin{matrix} \max \\ \min \end{matrix} \right\}\left(\mathbf{U}_1^*, \mathbf{U}_2^*, \ldots, \mathbf{U}_m^*\right). \tag{20}$$

The limit coefficients will be computed (see below) based on $P_i^\pm$ and the maximum and minimum increments and decrements the nodal solution values are allowed to achieve,

$$Q_i^\pm = \mathbf{U}_i^{\begin{matrix} \max \\ \min \end{matrix}} - \mathbf{U}^l. \tag{21}$$

Task Limit coefficients **(LIM)**

Defining the ratios of positive and negative element contributions for each node i that ensure monotonicity as

$$R_i^\pm = \begin{cases} \min\left(1, Q_i^\pm / P_i^\pm\right) & P_i^+ > 0 > P_i^- \\ 1 & \text{otherwise} \end{cases}, \tag{22}$$

the limit coefficient for each element is taken as the most conservative

ratio

$$C_e = \min_{i\in\Omega_e} \begin{cases} R_i^+ & \text{AEC} > 0 \\ R_i^- & \text{AEC} < 0 \end{cases}. \tag{23}$$

The limited AEC is then scatter-added to nodes

$$A_i = \sum_{i\in\Omega_e} C_e \cdot \text{AEC}. \tag{24}$$

Task Applying the limiter **(APPLY)**

The limited AEC is applied to the low-order solution according to Eq. (11),

$$U_i^{n+1} = U_i^l + A_i. \tag{25}$$

The above procedure is general, works on the numerical solution (instead on fluxes or slopes), and written as the same procedure for each scalar of a system of equations. This works well for independent scalars, but for a coupled system additional techniques have been developed to reflect the coupled nature of the equations in the limiting procedure, see also [3,4,9]. In particular, we have experimented with Löhner's 'indicator variable' approach, which designates a physical variable, e.g., density, whose limit coefficient other variables inherit in a cell, as well as applying a minimum of the limit coefficients for all or some of the conserved variables. These techniques tend to produce better results for some problems while worse for others – in any case, such a priori knowledge of the problem computed is beneficial towards obtaining improved numerical solutions.

5. Software design and implementation

This section discusses various software implementation details of the flow solver described in Section 4. The implementation uses Charm++ as the parallel programming paradigm. The entire problem, in this case the computational mesh, is broken up into multiple *chares*. Chares can be thought of as data and associated functions that operate on them, as in any object-oriented programming paradigm. In code, a chare is represented by a C++ class. Since each chare holds a different partition of the mesh and associated data, this is simply the realization of the divide and conquer paradigm. Chares communicate with each other via message passing. Up to this point there is nothing new or special compared to any other code relying on a distributed-memory paradigm, e.g., the message passing interface (MPI).

In the following sections we give a brief overview of the major features of the Charm++ runtime system, followed by discussion on those specific features, used by the flow solver, that significantly differentiate this from other distributed-memory implementations. Finally, the main steps of the algorithm and its implementation are outlined.

5.1. An overview of Charm++

Charm++ is a general-purpose production-grade many-tasking programming framework, runtime system, and ecosystem of libraries for modern high-performance computing systems, [10–14]. It offers high productivity and performance portability through features such as multicore and accelerator support, dynamic load balancing, fault tolerance, latency hiding, interoperability with MPI and OpenMP, and online job-resizing. Charm++ has been developed and maintained by the Parallel Programming Laboratory at the University of Illinois at Urbana-Champaign for 20+ years. It is similar to MPI in the sense that it allows writing high-performance applications for the largest distributed-memory computers. The important differences and main advantages of Charm++ over MPI are

- Fully asynchronous execution model, allowing arbitrary overlap of computation and communication
- Task-parallelism, scheduling parts of an algorithm independently of or dependent on each other
- Automatic load balancing, redistributing computational load by migration of work units based on real-time CPU load measurement
- Automatic checkpointing and fault tolerance, allowing restart with differing number of work units and resizing jobs on the fly instead of interruption
- Support for power-, and energy-aware computation, by intelligent work redistribution based on, e.g., CPU frequency scaling or temperature
- Interoperability with MPI, OpenMP, CUDA, from C++, Fortran, and Python

For more information on Charm++ see http://charmplusplus.org and for publications see http://charm.cs.illinois.edu/papers.

5.2. Communication with message passing in Charm++

In a Charm++ program, data and work-units (chares) interact via asynchronous function calls. Communication via message passing is realized by special class member functions, called *entry methods*. Entry methods differ from ordinary member functions in that they can be called remotely, by using the chare array handle addressed by the chare id and its member function to call. Function arguments to such entry methods can be of any standard or custom type. If the target of the chare happens to reside on a remote compute node, the runtime system serializes the function arguments into a byte stream, sends it across the network, unpacks it on the other side, and puts the function call into the local queue of the target processor. Different functionality (with associated data) is divided into a chare array of such objects, thus an algorithm is realized by a dynamically interacting arrays of chares. As an example, Listing 1 compares asynchronous message passing in MPI and Charm++, displaying code used to send and receive arrays whose size is only known at runtime and can be different on different chares/ranks, characteristic of unstructured-mesh solvers. In Charm++ point-to-point communication is done via such asynchronous entry-method function calls.

The implementation (declaration and definition) of entry-method member functions, such as `fn(...)` in Listing 1, do not differ in any way from usual C++ (non-entry) methods. Such functions are, however, labeled as entry methods in Charm++ *interface* files, commonly with extension `.ci`, as shown in Fig. 1. While the examples listed in Listing 1 send and receive a simple standard C++ vector (a contiguous-storage, dynamically-resizable, array), Charm++ also allows asynchronously sending and receiving arbitrarily complex custom-built data structures this way as well without measurable performance penalties, compared to floating-point calculations, as will be shown. Since the underlying programming paradigm of Charm++ is higher level than MPI + X (where X stands for some form of threading, e.g., OpenMP or CUDA), in Charm++ distributed-memory sends and receives may operate on (safe) custom data structures (instead of low-level byte-streams), e.g., containers built from C++ standard library vectors, trees, hash maps, or arbitrary user-defined data types. In Section 7 we demonstrate that communication using such high level data structures yields an insignificant performance hit compared to computation.

5.3. Problem decomposition in Charm++

It is important to appreciate that in Charm++ programs one usually does *not* address hardware elements, e.g., CPUs or threads. Instead, chare arrays elements have an ID, an integer by default. This makes sense, since the runtime system may migrate chares (and their data) from one compute node to another during computation to perform load balancing. Such migration is based on real-time load measurement and is transparent to the application. The runtime system dynamically and automatically adapts the computational load, monitoring load-

```
// Non-blocking send and receive with MPI, source: https://stackoverflow.com/a/14051503
if (rank == 0) {
  MPI_Request req;
  // Send a message to rank 1
  MPI_Isend(arr1, n, MPI_DOUBLE, 1, 0, MPI_COMM_WORLD, &req);
  // Do not forget to complete the request!
  MPI_Wait(&req, MPI_STATUS_IGNORE);
}
else if (rank == 1) {
  MPI_Status status;
  // Wait for a message from rank 0 with tag 0
  MPI_Probe(0, 0, MPI_COMM_WORLD, &status);
  // Find out the number of elements in the message -> size goes to "n"
  MPI_Get_count(&status, MPI_DOUBLE, &n);
  // Allocate memory
  arr1 = malloc(n*sizeof(double));
  // Receive the message. ignore the status
  MPI_Recv(arr1, n, MPI_DOUBLE, 0, 0, MPI_COMM_WORLD, MPI_STATUS_IGNORE);
}

// ------------------------------

// Non-blocking send and receive with Charm++
using namespace std;
// on rank 0: create & fill array a
vector<double> a{...};
// send array a
object[1].fn(a);
// on rank 1: receive array
void Object::fn( const vector<double>& a ) { // use array a }

// Member function labeled as a Charm++ entry method for receiving a
// variable-size array in a Charm++ interface file, Object.ci
array [1D] Object {
  entry void fn( const vector<double>& a );
};
```

Listing 1. Non-blocking send and receive of a variable-length array with MPI and Charm++.

imbalance, and can also migrate data and work-units if it notices that a compute node failed or is about to fail, enabling fault tolerance.

Similar to other distributed-memory solvers for unstructured meshes, after reading the mesh from computer file to memory, it is partitioned, usually by a coordinate-, or a graph-based partitioner. However, the number of mesh partitions does not have to equal the number of PEs. Experience shows that such *overdecomposition* (or *virtualization)*, i.e., significantly more work units (mesh partitions) than the available number of PEs, can be beneficial, especially with load balancing. While overdecompositon increases communication costs, it also comes with benefits: (1) useful computation happens on smaller mesh partitions which may improve cache utilization, and (2) finer-grain work units may be load-balanced more efficiently, as will be shown in Section 7.

5.4. MPI interoperation and processor-aware collections

The Charm++ paradigm is the single abstraction our implementation uses. We also rely on a number of third-party libraries some of which require MPI. This is not a problem with Charm++ as Charm++-code can seamlessly interoperate with MPI-only libraries. There are various ways Charm++ and MPI code can interact within a single

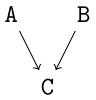


```
// DAG logic specified in Charm++ .ci file
array [1D] Object {
  entry void wait4c() {
    when a_complete(), b_complete() serial { c(); } };

  entry void a_complete();
  entry void b_complete();
};
```

Fig. 1. *Left:* Structured DAG expressing a simple logic of task `A` *and* `B` must finish before task `C` can start. *Right:* Charm++ SDAG code expressing the logic on the left. Here `a_complete()` and `b_complete()` are member functions of `Object` that are implemented by the runtime system, used to trigger the completion of task `A` and `B`, respectively. The runtime system monitors the completion of tasks `A` and `B`, and only when both are complete will it call member function `c()`.

application. We invoke library calls that contain direct MPI calls from Charm++ chare *groups*. Chare groups are similar to chare arrays with the important differences that there is a guaranteed single group element per physical processor and group elements never migrate. This enables invoking calls by MPI libraries from groups that otherwise know nothing about their environment.

In particular, the flow solver uses Zoltan2 [15] for initial mesh partitioning (which supports multiple types of partitioners in parallel as well as overdecomposition), and ExodusII [16] (used for mesh and field solution output to files in parallel). Using existing libraries thus allows building on the specific expertise of their authors.

Besides groups, another type of processor-aware chare collection in Charm++ is a *nodegroup*. Node groups are similar to groups (e.g., they do not migrate) but a node group is a collection of chares with one chare per *process* or *logical (e.g., compute) node*. Thus node groups allow writing code that must be executed on a compute-node basis. An example is *N*-to-*M* file I/O, which allows, for example, efficiently reading a large mesh from file to memory on $N \ll M$ (instead of *M*) compute nodes. This can be used to optimize I/O performance if *N* is the number of I/O nodes and *M* is the number of compute nodes on a large cluster. This is how our flow algorithm reads in its input computational mesh, which is followed by mesh partitioning and cell/node redistribution based on the output of the mesh partitioner.

5.5. Task-parallelism

Task-parallelism is a parallel programming technique used to express parts of an algorithm as a graph of connected or independent tasks. Besides the ubiquitous divide-and-conquer (data-parallelism), task-parallelism has been recently gaining popularity [17], complementing data-parallelism, to increase the degree of overlap among various tasks of an algorithm.

In Charm++ task-parallelism is expressed via its *structured DAG* (SDAG) functionality, where *DAG* stands for Direct Acyclic Graph. DAGs are used to identify dependencies among individual tasks of an algorithm, represented by graph nodes. A DAG in Charm++ is expressed by a simple language extension, specified in the Charm++ interface (`.ci`) file, that allows expressing the logic of interdependence among tasks. There may be different and multiple DAGs within a Charm++ chare array (class) definition. Each array element represents a different C++ class instance, holding its own data, e.g., a partition of the computational mesh and the solution. Execution of the algorithm within a single chare object instance is generally independent of execution within another chare array element.

An example of a simple DAG may consist of tasks `A`, `B`, and `C`. Then if task `A` *and* `B` must both finish before `C` can be started, a DAG that expresses this logic within Charm++ is given in Fig. 1. Besides separating `*_complete()` member functions by a comma, SDAG constructs also support more advanced control flow specifiers, such as `for`, `while`, and `case` statements. Using Charm++ SDAG code, fairly complex application logic can be expressed.

5.6. Flow algorithm software design using Charm++: setup

We are now in a position to describe the main steps of the flow algorithm in Section 4. The setup consists of the following main steps:

1. Read user input (from command-line arguments and an input text file)
2. Read the mesh in parallel (one linear chunk per compute node from a single file)
3. Pass the linearly-distributed mesh to a mesh partitioner allowing overdecomposition
4. Redistribute the mesh (cell connectivity and coordinates) based on the distribution from the partitioner
5. Compute nodal communication maps in parallel
6. Create migratable chare arrays holding a mesh partition (connectivity, coordinates, nodal communication map, and solution arrays)

Except for Step 1 above, all steps are parallel and no assumption is made on the size of the input mesh, e.g., that it must fit into the memory of a single compute node. All steps above are common in distributed-memory implementations of unstructured-mesh solvers, except our Charm++ implementation is fully asynchronous and puts data in migratable chare arrays. In the following we describe Step 5 in some detail, since a scalable distributed-memory implementation of computing the nodal communication maps appears less than straightforward with the constraint that the mesh cannot be loaded to a single compute node's memory.

5.7. Computing the nodal communication maps in parallel

Until Step 5 during setup, only the mesh connectivity graph and the node coordinates are known on each chare. From this information our task in Step 5 is to compute the nodal communication map in a scalable fashion in parallel. No information is available on which chare might store the list of nodes that other chares share and we cannot assume that the entire mesh can fit into the memory of a single compute node. Any approach that singles out a master communicating with slaves will not scale. Additionally, we would like to minimize the amount of data that must be sent across the network during setting up the node communication map. A nodal communication map on each partition (chare) is required for any distributed-memory unstructured-grid solver that stores the solution unknowns at mesh nodes. On each chare such a map

$//storage\ for\ nodal\ communication\ map\ for\ each\ chare\ (mesh\ partition)$
$std :: unordered\_map < int, std :: vector < int >> nodeCommMap;$

associates a list of node IDs to a chare ID a given chare shares nodes with. The map must store a (different) list of nodes for each of potentially multiple other chares it shares at least a single node with. Using the standard library in C++ such a map can be implemented using a map of vectors:At this point, the node communication map, \begin{verbatim} nodeCommMap\end{verbatim} is a dynamic but empty *unordered* (hash) map. Unordered maps are standard associative containers in C++ that contain key-value pairs with unique keys. In the map the keys are the chare IDs the given chare shares a list of nodes with and associated to each key (the value) is a vector of integers (a standard, continuous-storage, resizable array that knows its size). Search, insertion, and removal of elements of unordered maps have guaranteed average constant-time algorithmic complexity. Internally in a hash map, the elements are not sorted in any particular order, but organized into buckets. Which bucket an element is placed into depends entirely on the hash of its key. This allows fast access to individual elements, since once the hash is computed, it refers to the exact bucket the element is placed into. This is an efficient data structure for dynamically and frequently changing data.

5.7.1. Step 1: query

One way to accomplish computing the nodal communication map in a distributed-memory setting that is scalable and performant is to build the map in two steps: (1) *query* and (2) *response*. Before the query each chare collects a list of boundary nodes from its mesh partition. A node is on a chare boundary if it belongs to a face of a tetrahedron that has no neighbor element at one of its faces. The list of boundary nodes can be computed using an algorithm that relies on standard data structures, e.g., elements surrounding points, derived from unstructured meshes [3,18]. Once the boundary nodes are computed, they are categorized into bins that will be sent to different chares to build the node communication map across all chares. The binning is determined by the node IDs and assigned to chares in a linear fashion. The nodes in each bin are then sent to the chare a given bin is assigned to. Note that the nodes in the bins are independent of their final destination: the target chare will merely be responsible for assembling the communication map for the list of nodes in the bins it is responsible for. Sending and receiving the node lists in bins avoid expensive collectives that would involve all chares and only entail point-to-point communication with data involving only a subset of the mesh boundary nodes. Since the boundary nodes are uniquely assigned to bins, no boundary node is sent to multiple chares, which keeps communicated data to a minimum. The chares receiving the boundary nodes in bins store them in two maps that are the inverse of each other:

```
// Storage for sending back categorized communication maps. Outer key: target
// chare, inner key: chare neighboring the target chare, value: unique set of
// nodes shared with neighbor chare.
std::unordered_map< int, std::map< int, std::unordered_set<int> > > exp;

// Compute node communication map to be sent back to chares
for (const auto& [neighborchare,bndnodes] : chnode) {
  auto& e = exp[neighborchare];       // insert neighbor chare ID as outer key
  for (auto n : bndnodes)             // for all boundary nodes of neighbor chare
    // find and loop over all boundary nodes in node->chare map
    for (auto d : find_value_of(m_nodech,n))
      if (d != neighborchare)
        e[d].insert(n);
}

// Send node communication maps to chares that issued a query to this chare
for (const auto& [ targetchare, bndnodes ] : exp)
  thisProxy[ targetchare ].bnd( thisIndex, bndnodes );
```

Listing 2. *Response* step following the *query* step in building the nodal communication maps. Besides showing the algorithm used to categorize the nodal communication maps by target and neighbor chares, this listing is also an example of how sending a complex data structure using Charm++ looks like in verbatim, i.e., *not pseudo*, code: The last two lines perform a `for` loop to send, in a point-to-point fashion, an integer (the sender chare ID, `thisIndex`) and the nodal communication map needed by `targetchare`, `bndnodes`, a `std::map` whose key is an integer and value is a hash set. Here `std::map` is a standard *sorted* associative container that contains key-value pairs with unique keys. Keys are sorted by using a comparison function. Search, removal, and insertion operations in such maps have logarithmic complexity as maps are usually implemented as red-black trees. The `std::unordered_set` (or hash set) is also a standard C++ associative container that contains a set of unique objects of type of its key. Search, insertion, and removal in such sets have average constant-time complexity. Internally, in unordered sets the elements are *not sorted* in any particular order, but organized into buckets. Which bucket an element is placed into depends entirely on the hash of its value. This allows fast access to individual elements, since once a hash is computed, it refers to the exact bucket the element is placed into.

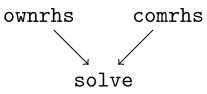


```
// DAG logic specified in diagcg.ci
array [1D] DiagCG {
  entry void wait4rhs() {
    when ownrhs_complete( tk::Fields& dif ), comrhs_complete()
    serial { solve( dif ); } }

  entry void ownrhs_complete( tk::Fields& dif );
  entry void comrhs_complete();
};
```

Fig. 2. *Left:* Structured DAG expressing the logic of computing and communicating the RHS and the mass diffusion term. Both `ownrhs` *and* `comrhs` must finish before `solve` can start. *Right:* Charm++ SDAG code expressing the logic on the left. Only when both own and contributions to the boundary nodes are complete on a given chare will the runtime system call the member function `solve()`. Note the function argument passed to `ownrhs_complete()`. This is allowed by Charm++ even though the runtime system implements the body of this function. This is used here to pass through the diffusion term `dif` directly to the `DiagCG::solve()`, which avoids having to store this data in `DiagCG`'s state, reducing its size, which is advantageous for migration as well as check point/restart.

$$//Node->chare\ map$$
$$std::unordered\_map<int, std::vector<int>>\ nodech;$$
$$//Chare->node\ map,\ the\ inverse\ of\ nodech$$
$$std::unordered\_map<int, std::vector<int>>\ chnode;$$

where nodech associates chares (value) to nodes (key), while chnode associates nodes (value) to chares (value). These data structures are small, temporary, and will be thrown away after the *response* step.

5.7.2. Step 2: response

Once all chares have received their assigned bins, the *response* step starts by computing the communication map for each boundary node. Since `nodech` and `chnode` only contain data on queried nodes and this data originates from source chares that have these nodes, these inverse maps already contain the communication maps that we need. Thus we only have to categorize the maps by source chare. The *response* step is given in Listing 2. The algorithm categorizes the nodal communication maps by the querying source chare and prepares the hash map `exp` for sending the maps back. The syntax uses C++ structured bindings and range-based for loops for readability; note that this is actual code lifted from the source. The last step in Listing 2 is to send the categorized maps back to the source chares. The object `thisProxy` is a Charm++ handle to the Charm++ chare array collection this code is implemented in. Using array-like indexing into the collection itself, `thisProxy[targetchare].bnd(...)` makes a call to the target chare array element and invokes its member function `bnd()`, an entry method, packing its arguments and sending them across the network if the `targetchare` happens to be on another compute node. Here `thisIndex` stands for the chare ID of the sender, so that the receiver knows where the contribution came from. The communication step in the *response* step is similar to that of in *query*, point-to-point and sending minimal data for boundary nodes. Node communication maps are computed only for those chares that queried the map from the given responding chare. The boundary nodes can also be thought of as a distributed table and each chare only works on a chunk of it. Note that a chare only sends data back to those chares that have queried the chare.

5.8. Flow algorithm software design using Charm++: time stepping

The last step of the setup phase, enumerated in Section 5.6, is to create the Charm++ chare arrays, designed to perform the time stepping. These chare arrays are migratable and *bound*. Bound arrays in Charm++ always migrate together while allowing separating different functionality and associated data. The important chare classes that interoperate during time stepping are

- `Transporter` (single chare, driver),
- `Discretization` (chare array, generic unstructured-grid solver base class),
- `DiagCG` (chare array, child class to `Discretization`, specialized to the node-centered continuous Galerkin finite element discretization scheme with a lumped-mass left-hand side and flux-corrected transport combined with Lax–Wendroff-like explicit time stepping scheme, discussed in this paper), and
- `DistFCT` (chare array for distributed-memory flux-corrected transport, used by `DiagCG`)

The base `Discretization` and child `DiagCG` classes facilitate the well-known object-oriented design feature, runtime polymorphism. This enables code reuse and helps code generic to all types of discretizations stay uniform and code specific to a given discretization stay modular. Such a design is particularly useful when more than a single type of hydrodynamics schemes are implemented in a single code, as is our case, since we have multiple co-existing continuous (node-centered) as well as discontinuous (cell-centered) Galerkin finite element methods, [19]. The base class Charm++ chare array, `Discretization`, encapsulates data and member functions that are generic to all unstructured-grid-based discretization schemes. Its array elements store, in a distributed fashion, the mesh connectivity and node coordinates. As `Discretization` is a chare array, its elements are distributed across the whole problem on all available compute nodes and PEs, and can also migrate for load balancing. The child class `DiagCG` is also a chare array, whose elements store the unknown solution at mesh nodes and implements the particular discretization scheme, discussed in Section 4. The elements of `DiagCG` are bound to those of `Discretization`. This enables accessing data associated to the same problem partition, e.g., the mesh, by the child from the base using a raw pointer, since bound elements always migrate together during load balancing. Additionally, `DistFCT` is also bound to `Discretization` and `DiagCG`.

With the above and Section 4 in mind, time stepping is preceded by (1) setting initial conditions and (2) computing the left hand side (task `LHS`). As discussed in Section 4.4, if the mesh does not change, the left hand side does not have to be recomputed during time stepping. A single time step consists of the following steps:

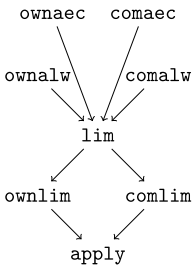


```
// DAG logic specified in distfct.ci
array [1D] DistFCT {
  entry void wait4fct() {
    when ownaec_complete(), comaec_complete(),
         ownalw_complete(), comalw_complete() serial { lim(); } };

  entry void wait4app() {
    when ownlim_complete(), comlim_complete() serial { apply(); } };

  entry void ownaec_complete();
  entry void ownalw_complete();
  entry void ownlim_complete();
  entry void comaec_complete();
  entry void comalw_complete();
  entry void comlim_complete();
};
```

Fig. 3. *Left:* Structured DAG expressing the logic of computing and communicating the nodal vectors, $\mathbf{P}^{\pm}$, $\mathbf{Q}^{\pm}$, $\mathbf{A}$, required in the flux-corrected transport algorithm. As the top portion of the DAG instructs, *all* of `ownaec`, `comaec`, `ownalw`, *and* `comaec` must finish before `lim` can start. Task `lim` then spawns two tasks, `ownlim` and `comlim`, which *both* must complete before `apply` can be executed. *Right:* Charm++ SDAG code expressing the logic on the left. Only when both own and contributions to the boundary nodes for both $\mathbf{P}^{\pm}$ *and* $\mathbf{Q}^{\pm}$ are complete on a given chare will the runtime system call the member function `lim()`. Only when both own and contributions to the boundary nodes for $\mathbf{A}$ are complete on a given chare will the runtime system call the member function `apply()`.

1. Compute the size of the next time step, Δt
2. Communicate Δt to all chares, performing a parallel all-to-all `min()` operation
3. Compute local contributions to RHS and $\mathbf{d}$, spawning tasks `RHS` and `DIF`, see Eqs. (9) and (16)
4. Communicate the RHS and $\mathbf{d}$, summing contributions to boundary nodes
5. When all contributions of RHS and $\mathbf{d}$ are ready on a chare, solve both the high-, and low-order system
6. Compute the nodal $\mathbf{P}^{\pm}$ and $\mathbf{Q}^{\pm}$, spawning tasks `AEC` and `ALW`
7. Communicate contributions of $\mathbf{P}^{\pm}$ and $\mathbf{Q}^{\pm}$ across boundary nodes
8. When all contributions to $\mathbf{P}^{\pm}$ and $\mathbf{Q}^{\pm}$ are ready on a chare, spawning task `LIM`, compute the limit coefficients, C_e, scatter-adding the limited AEC to nodes
9. Communicate the limited AEC in nodes on the boundary
10. When all contributions of the limited AEC are ready on a chare, apply the limited AEC on the low order solution, Eq. (25)
11. Evaluate load imbalance and migrate if necessary
12. Continue with Step 1, starting a new time step

Steps 6–9 and computing $\mathbf{d}$ in Step 3 are performed by the bound `DistFCT` array elements while the rest by `DiagCG`. It is important to appreciate that during all steps, every chare array element holds and works on its own mesh partition and also has its own task state, which is different from the state of another chare. Chares communicate, in a point-to-point fashion, with their handful of neighbors, those that they share chare-boundary nodes with, see Section 5.7. As a result, no synchronization is necessary beyond what is prescribed by the task graphs (discussed in detail below), except computing the new time step size, which is the single collective within a time step. This provides considerable freedom for the runtime system to schedule tasks and overlap computation and communication, constantly monitoring real-time CPU-load and communication patterns. The system can also dynamically adapt to external factors influencing computation, e.g., CPU frequency scaling due to temperature deviations and temporarily (or notoriously) underperforming compute nodes, usually out of control of both developers and users.

Table 1
Mesh sizes for convergence studies. Here K stands for thousand, M for million, and h is the average edge length.

Mesh	Points	Tetrahedra	h
0	132651	750 K	0.02
1	1030301	6 M	0.01
2	8120601	48 M	0.005

Steps 3–5: Fig. 2 shows the DAG and Charm++ code that express the logic behind Steps 3–5, the first computation/communication steps in a time step. The DAG is simple and prescribes that only when both own and contributions to the boundary nodes are complete on a given chare should the runtime system call the member function `solve()`, which computes both high-, and low-order (unlimited) solutions, $\mathbf{U}^l$ and $\Delta\mathbf{U}^h$. As the DAG does not assume a particular ordering between the tasks `ownrhs` and `comrhs`, either can execute first or second and this order can also differ on different chares, working on different mesh partitions. As a result, the different tasks cannot assume being the first writing to a particular data array they operate on. The own and communicated portions of the RHS are buffered into arrays that are different from the ones in which the owned portions are stored. The own and communicated contributions are then combined in `solve()`, at different times on different chares, when a chare is ready to call this function, independent of other chares.

Steps 6–10: Fig. 3 shows the DAG and Charm++ code that expresses the logic behind Steps 6–10, the limiting step. The individual tasks of the limiting procedure are discussed in Section 4.4. These are `LHS`, `RHS`, `DIF`, `AEC`, `ALW`, `LIM`, and `APPLY`. Tasks `RHS` and `DIF` have been already performed simultaneously in Steps 3–5 using the DAG in Fig. 2. Thus the limiting procedure involves the remaining tasks. Three intermediate nodal vectors are required for computing the limited high-order solution: the sum of all positive and negative AEC to nodes, $\mathbf{P}^{\pm}$, Eq. (17), the maximum and minimum increments and decrements the nodal solutions values are allowed to achieve, $\mathbf{Q}^{\pm}$, Eq. (21), and the limited AEC applied to nodes, $\mathbf{A}$, Eq. (24). Besides the slightly more complex task logic, there is nothing new in Fig. 3 not encountered before: ordering among the edges of the graph is not assumed and thus the tasks must only write to disjoint data, which then are combined before used. `DistFCT::apply()` then calls back to `DiagCG` which applies the now combined limited AEC, updates the high-order solution, and continues by telling the runtime system to evaluate the degree of load imbalance across the whole problem which performs migration if necessary. A number of different load balancing strategies are available in Charm++, which can be configured simply by passing a different command line argument to the executable. A crucial point is that we simply turn on load balancing and the runtime system performs CPU load measurement and object migration if necessary, building on decades of research, expertise, and experience in load balancing strategies. When load balancing is finished, a member function is called on each chare, continuing to the next time step.

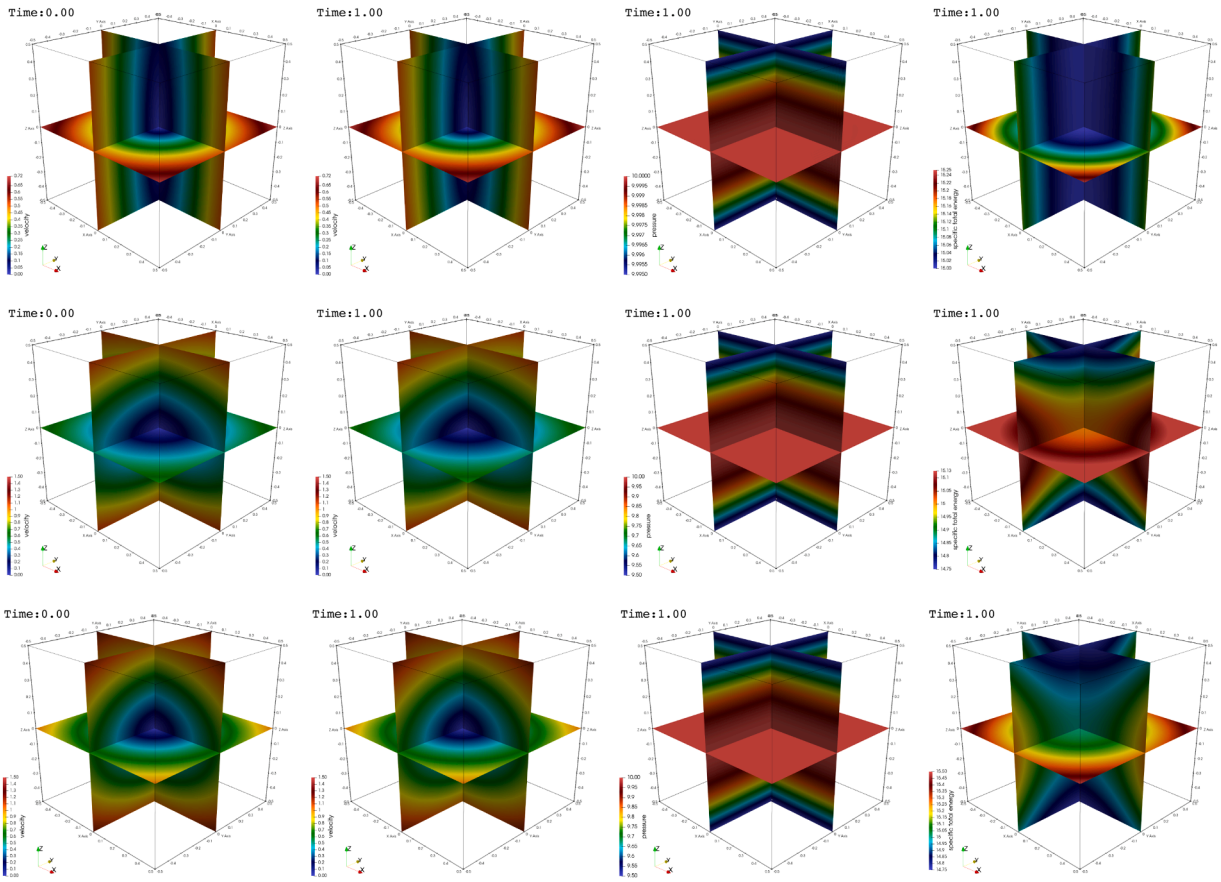

Fig. 4. Initial (first column) and final (second column) velocity, pressure (third column), and total energy distributions (fourth column), for $\alpha = 0.1$ and $\beta = 1.0$ (top row), $\alpha = 1.0$ and $\beta = 0.1$ (middle row), and $\alpha = \beta = 1.0$ (bottom row) for the vortical flow problem.

Table 2
L_2 errors and convergence rates for the vortical flow problem with $\alpha = \beta = 1$.

Mesh	$L_2(\rho)$	$L_2(\rho u_1)$	$L_2(\rho u_2)$	$L_2(\rho u_3)$	$L_2(\rho E)$
750K	1.31×10^{-5}	2.91×10^{-5}	1.24×10^{-5}	1.52×10^{-4}	6.29×10^{-5}
6M	3.23×10^{-6}	6.80×10^{-6}	2.67×10^{-6}	3.58×10^{-5}	1.67×10^{-5}
48M	8.00×10^{-7}	1.63×10^{-6}	6.30×10^{-7}	8.05×10^{-6}	4.18×10^{-6}
p	2.01	2.06	2.08	2.15	2.00

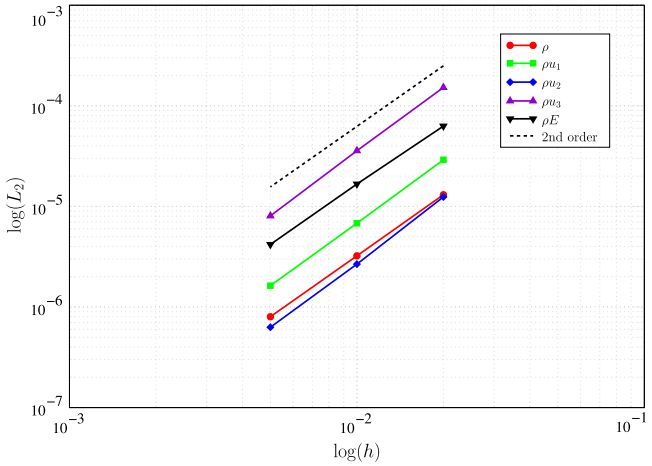

Fig. 5. L_2 errors as a function of mesh resolution for the vortical flow problem.

6. Solution verification

This section presents test problems used to verify the accuracy and the correctness of the implementation of the numerical method. As expected, the method is 2nd-order accurate for smooth problems.

We adopt a number of test problems that have been derived in [20,21] using the method of manufactured solutions for the Euler equations that yield smooth solutions. Since the analytical solution for these problems are known, the numerical errors can be quantified. The errors are also used to establish the order of accuracy of the method. Convergence studies for each problem were performed with a series of finer meshes over a unit cube as the computational domain centered at the origin. Note that these are the same meshes that were used in [21]. The meshes were constructed from a collection of uniform hexahedra that were further subdivided into approximately uniform tetrahedra. Table 1 summarizes the three meshes used including the number of points, number of tetrahedra, and average edge length, h.

The global L_2 error in each field variable was calculated as

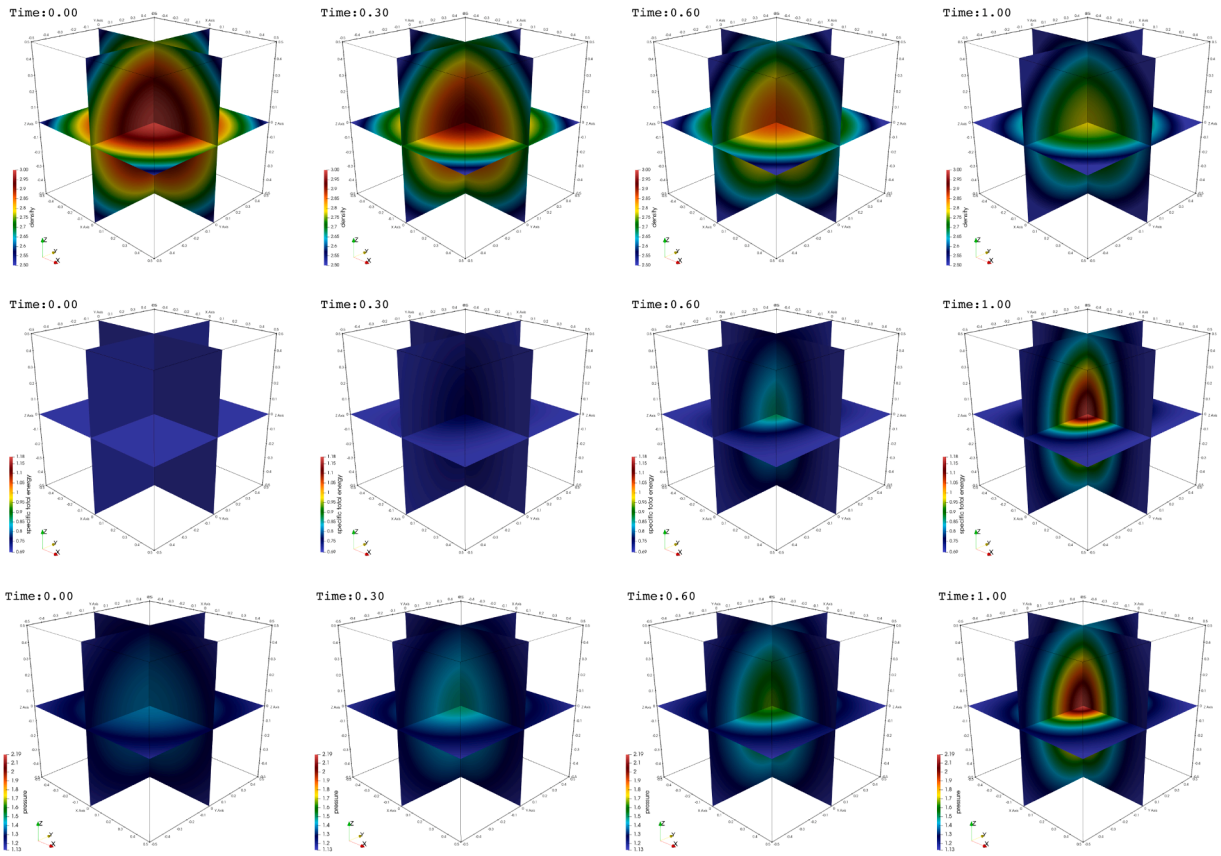

Fig. 6. Density (top row), energy (middle row), and pressure (bottom row) distributions on center planes at four different simulation times (columns) for the nonlinear energy growth problem.

$$||\varepsilon||_2 = \frac{\sum_{v=1}^{n} M_l^v \left(\widehat{U}^v - U^v\right)^2}{\sum_{v=1}^{n} M_l^v} \tag{26}$$

where n is the number of points, $\widehat{U}^v$ and U^v are the exact and computed solutions at mesh point v, and M_l^v is the lumped mass matrix, i.e., volume, associated to mesh point v. The convergence rate $\mathbf{p}$ was then calculated as

$$\mathbf{p} = \frac{\log||\varepsilon||_2^{m+1} - \log||\varepsilon||_2^{m}}{\log h^{m+1} - \log h^{m}} \tag{27}$$

where m is a mesh index.

6.1. Vortical flow

The purpose of this problem is to test velocity errors generated by spatial operators in the presence of 3D vorticity and in particular the superposition of planar and vortical flows, analogous to vorticity stretching. The derivation of this test problem is given in [21], preceded by a simplified version published in [20]. The combination of vorticity and velocity gradients is a fundamental source of kinetic energy in flows that transition to shear-driven turbulence, and hence an important ingredient of computing many practical engineering and atmospheric flows. The analytical solution is

$$\begin{aligned} \rho &= 1 \\ u_i(x_i) &= \begin{pmatrix} \alpha x - \beta y \\ \beta x + \alpha y \\ -2\alpha z \end{pmatrix} \\ p(z) &= p_0 - 2\rho\alpha^2 z^2 \\ e &= p(z)\rho(\gamma - 1), \end{aligned} \tag{28}$$

and the source terms, in Eq. (1), are

Table 3
L_2 errors and convergence rates for the nonlinear energy growth problem.

Mesh	$L_2(\rho)$	$L_2(\rho u_1)$	$L_2(\rho u_2)$	$L_2(\rho u_3)$	$L_2(\rho E)$
750K	7.67×10^{-4}	1.61×10^{-4}	1.08×10^{-4}	6.98×10^{-5}	3.39×10^{-4}
6M	2.01×10^{-4}	3.84×10^{-5}	2.67×10^{-5}	1.63×10^{-5}	7.97×10^{-5}
48M	5.57×10^{-5}	9.38×10^{-6}	6.59×10^{-6}	3.90×10^{-6}	1.97×10^{-5}
p	1.85	2.03	2.02	2.06	2.02

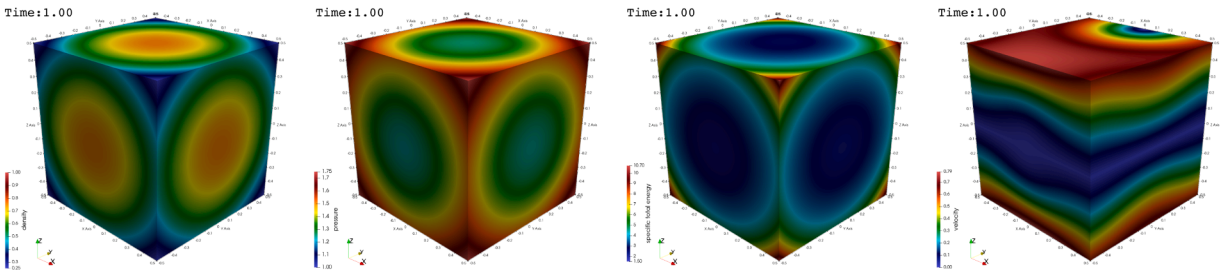

Fig. 7. Density, pressure, energy, and velocity on the surface at the final simulation time for the Rayleigh–Taylor unstable configuration.

$$
\begin{aligned}
S_\rho &= 0 \\
S_{u,i} &= \begin{pmatrix} \rho(\alpha^2-\beta^2)x - 2\rho\alpha\beta y \\ \rho(\alpha^2-\beta^2)y + 2\rho\alpha\beta x \\ 0 \end{pmatrix} \\
S_E &= u_i S_{u,i} + \frac{8\rho\alpha^3 z^2}{\gamma - 1}.
\end{aligned}
\tag{29}
$$

The above solution was evolved for a single time unit using $\gamma = 5/3$, $p_0 = 10$, and $\rho = 1$ with three sets of parameters:

1. $\alpha = 0.1$, $\beta = 1$. This case corresponds to a predominantly vortical flow with a small amount of flow to and from the origin.
2. $\alpha = 1$, $\beta = 0.1$. This case corresponds to a weak vortex with strong flow away from the origin in the $x - y$ plane and toward the origin in the z-direction.

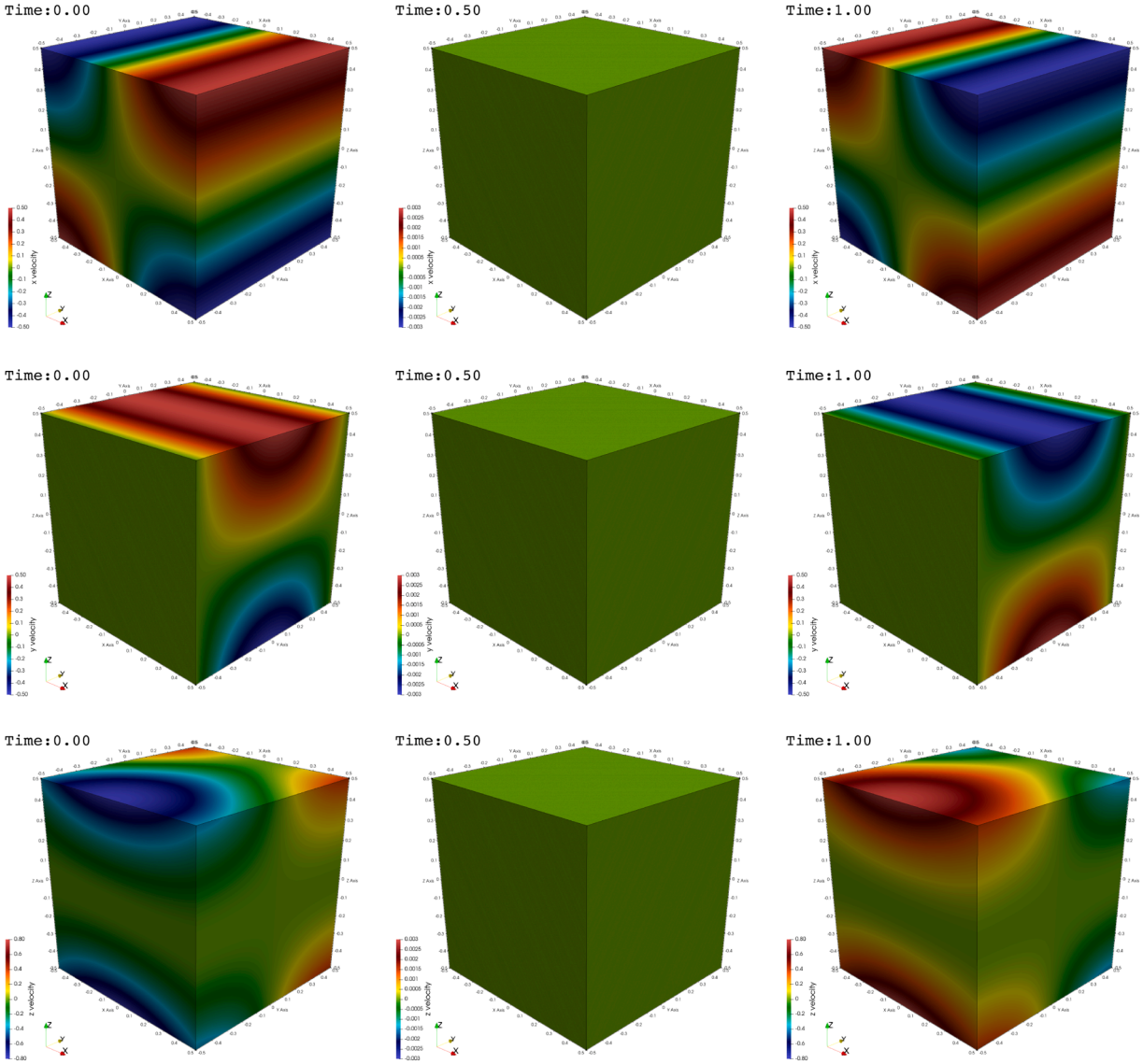

Fig. 8. Velocity components on the surface at three different simulation times ($t = 0$, 0.5, and 1.0) for the Rayleigh–Taylor unstable configuration. The velocity reverses direction over the indicated time interval.

Table 4
L_2 errors and convergence rates for the Rayleigh–Taylor problem.

Mesh	$L_2(\rho)$	$L_2(\rho u_1)$	$L_2(\rho u_2)$	$L_2(\rho u_3)$	$L_2(\rho E)$
750K	4.50×10^{-4}	6.04×10^{-4}	6.46×10^{-4}	4.22×10^{-5}	3.35×10^{-4}
6M	1.38×10^{-4}	1.84×10^{-4}	1.92×10^{-4}	1.28×10^{-5}	8.29×10^{-5}
48M	4.22×10^{-5}	5.58×10^{-5}	5.49×10^{-5}	3.98×10^{-5}	2.12×10^{-5}
p	1.71	1.72	1.81	1.69	1.97

3. $\alpha = \beta = 1$. This case is effectively a superposition of the previous two, with vortical flow comparable in strength to the flow to and from the origin.

Fig. 4 shows the initial and final velocity fields for each variant on center planes through the origin, which confirms the steady state nature of the problem. Also shown are the steady state pressure and energy fields. For the third case, Table 2 gives the L_2 errors in the computed conserved quantities along with the measured convergence rates. A time step of 0.002 was used for the coarsest mesh and successively halved for the finer meshes. Fig. 5 shows the log of the L_2 errors as a function of the log of the average edge length. The measured convergence rate in all variables is approximately 2.0, as expected.

6.2. Nonlinear energy growth

The purpose of this problem is to test nonlinear, time-dependent energy growth and the subsequent development of pressure gradients due to coupling between the internal energy and the equation of state. This flow represents a basic physics component of any type of explosion, in which internal energy is converted to pressure gradients without the complicating effects of fluid momentum and kinetic energy. The derivation of this test problem is given in [21]. The analytical solution is

$$\begin{aligned} \rho(x_i,t) &= \rho_0 + \exp(-\alpha t)g(x_i) \\ u_i(x_i) &= 0 \\ p &= [\rho_0 + \exp(-\alpha t)g](\gamma-1)\left(-3c_e - 3kh^2t\right)^{-1/3} \\ e &= \left(-3c_e - 3kh^2t\right)^{-1/3} \end{aligned} \tag{30}$$

with

$$\begin{aligned} g(x_i) &= 1 - \left(x^2+y^2+z^2\right) \\ h(x_i) &= \cos(\beta_x\pi x)\cos\left(\beta_y\pi y\right)\cos(\beta_z\pi z), \end{aligned} \tag{31}$$

and the source terms, in Eq. (1), are

$$\begin{aligned} S_\rho &= -\alpha\exp(-\alpha t)g \\ S_{u,i} &= 2kht[\rho_0 + \exp(-\alpha t)g](\gamma-1)\left(-3c_e - 3kh^2t\right)^{-4/3}\frac{\partial h}{\partial x_i} \\ &\quad + \left(-3c_e - 3kh^2t\right)^{-1/3}(\gamma-1)\exp(-\alpha t)\frac{\partial g}{\partial x_i} \\ S_E &= \rho kh^2e^4 + eS_\rho. \end{aligned} \tag{32}$$

Simulations of this problem were performed with the following parameters:

$$\rho_0 = 2;\ \alpha = 0.25;\ \kappa = 0.8;\ \beta_i = (1.0, 0.75, 0.5);\ c_e = -1 \tag{33}$$

The solution was evolved over a single time unit with $\gamma = 5/3$. A time step of 0.001 was used for the coarsest mesh and successively halved for the finer meshes. Fig. 6 shows the density, energy, and pressure distributions at four different times on center planes through the origin. Table 3 gives the L_2 errors in the conserved quantities computed along with the measured convergence rates. The measured convergence rate in all variables is approximately 2.0, consistent with expectations.

6.3. Rayleigh–Taylor unstable configuration

The purpose of this test case is to assess time-dependent fluid motion in the presence of Rayleigh–Taylor unstable conditions, i.e., opposing density and pressure gradients. The Rayleigh–Taylor instability is a basic feature of mixing flows with materials of different densities and the onset of turbulent flows that are very different from shear-driven flows [22]. Rayleigh–Taylor turbulence is induced by differences in material densities, reacting very differently to pressure gradients, characterized by a continuous conversion of potential to kinetic energy, yielding non-equilibrium flow (in which the production and dissipation of turbulent kinetic energy is not in balance), statistically non-stationary energy spectra, and anisotropy even at the smallest scales [23]. The derivation of this test problem is given in [21]. The solution is

$$\begin{aligned} \rho(x) &= \rho_0 - \left(\beta_x x^2 + \beta_y y^2 + \beta_z z^2\right) \\ u_i(x_i,t) &= f(t)g(x_i) = \cos(k\pi t)\begin{pmatrix} z\sin(\pi x) \\ z\cos(\pi y) \\ -\frac{1}{2}\pi z^2[\cos(\pi x) - \sin(\pi y)] \end{pmatrix} \\ p(x) &= p_0 + \alpha\left(\beta_x x^2 + \beta_y y^2 + \beta_z z^2\right) \\ E &= \frac{p}{\rho(\gamma-1)} + \frac{1}{2}f^2 g_i g_i \end{aligned} \tag{34}$$

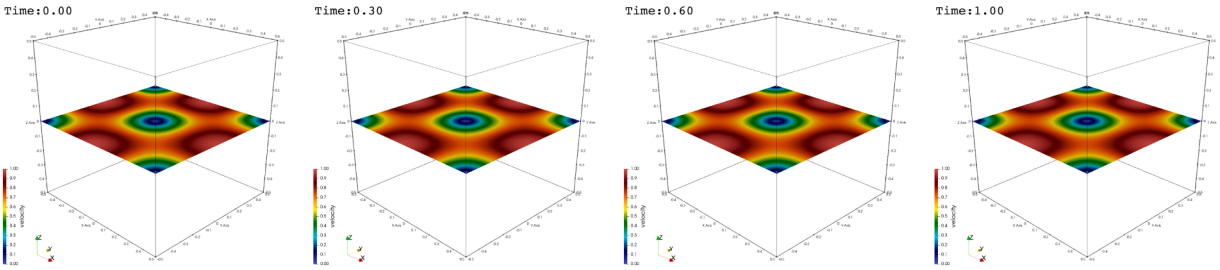

Fig. 9. Velocity magnitudes at a center plane at different simulation times for the Taylor–Green test problem.

Table 5
L_2 errors and convergence rates for the Taylor–Green problem.

Mesh	$L_2(\rho)$	$L_2(\rho u_1)$	$L_2(\rho u_2)$	$L_2(\rho u_3)$	$L_2(\rho E)$
750K	1.14×10^{-5}	8.56×10^{-5}	4.59×10^{-4}	2.64×10^{-5}	2.49×10^{-4}
6M	2.34×10^{-6}	1.62×10^{-5}	8.72×10^{-5}	4.40×10^{-6}	5.84×10^{-5}
48M	5.65×10^{-7}	3.17×10^{-6}	1.77×10^{-5}	9.10×10^{-7}	1.42×10^{-5}
p	2.05	2.35	2.30	2.27	2.04

and the source terms, in Eq. (1), are

$$
\begin{aligned}
S_\rho &= u_i \frac{\partial \rho}{\partial x_i} \\
S_{u,i} &= \rho g_i \frac{\partial f}{\partial t} + f g_i S_\rho + \rho f^2 g_j \frac{\partial g_i}{\partial x_j} + \frac{\partial p}{\partial x_i} \\
S_E &= \rho g_i g_i f \frac{\partial f}{\partial t} + \left[\frac{p}{\rho(\gamma-1)} + \frac{1}{2} f^2 g_i g_i \right] S_\rho \\
&\quad + \rho f g_i \left[\frac{1}{\rho(\gamma-1)} \frac{\partial p}{\partial x_i} - \frac{p}{\rho^2(\gamma-1)} \frac{\partial \rho}{\partial x_i} + f^2 g_j \frac{\partial g_j}{\partial x_i} \right] + f g_i \frac{\partial p}{\partial x_i}.
\end{aligned}
\tag{34a}
$$

The solution was evolved over a single time unit with $\gamma = 5/3$. A time step of 0.001 was used for the coarsest mesh and successively halved for the finer meshes. Fig. 8 depicts the velocity field at the surface at different simulation times, showing the reversal of the velocity components in time, indicating the spatial and temporal dynamics of the velocity field. Fig. 7 shows density, pressure, energy, and velocity on the surface at the final simulation time. Table 4 gives the numerical L_2 errors in the conserved quantities computed. The order of convergence approaches the expected value of 2.0.

6.4. Taylor–Green vortex

3D simulations of the 2D Taylor–Green vortex, see e.g., [24], were performed using the same meshes as for the other test problems described above. A similar configuration was also computed in [20] and [25] on a different, practically 2D, domain. The Taylor–Green vortex problem is commonly used to examine transition to turbulence from a well-characterized initial state. The initial conditions consists of a regular pattern of sinusoidal variation in x-, and y-velocities, with the pressure satisfying a Poisson equation of incompressible flows and with constant density at all times. For the case of constant-density fluid,

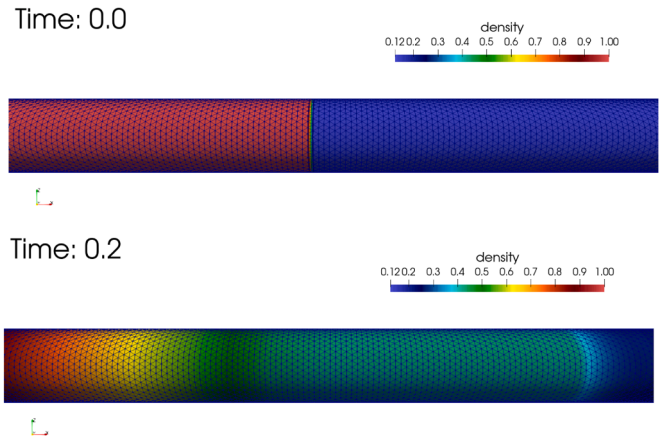

Fig. 10. Surface mesh colored by density at $t=0$ and $t=0.2$ on mesh 1 for the Sod shock tube problem.

Taylor and Green [26] describe a semi-analytic solution suitable for early times. For the compressible case no exact solution is known, but this problem is widely-used as a test of multi-dimensional hydrodynamics of disordered flow. Enforcing constant-density, the following solution

$$
\begin{aligned}
\rho(x) &= 1 \\
u_i(x_i, t) &= \begin{pmatrix} \sin\pi x \cos\pi y \\ -\cos\pi x \sin\pi y \\ 0 \end{pmatrix} \\
p(x) &= 10 + \frac{1}{4}\rho(\cos 2\pi x + \cos 2\pi y) \\
e &= \frac{p(x)}{\rho(\gamma-1)}
\end{aligned}
\tag{35}
$$

is maintained in a steady state by the compressible-flow solver with the source terms

$$
\begin{aligned}
S_\rho &= 0 \\
S_{u,i} &= 0 \\
S_E &= \frac{3\pi}{8}(\cos\pi x \cos 3\pi y - \cos 3\pi x \cos y).
\end{aligned}
\tag{36}
$$

This test problem was also run for a single time unit with $\gamma = 5/3$. A time step of 0.002 was used for the coarsest mesh and successively halved for the finer meshes. Fig. 9 shows the velocity magnitudes across a center plane at different simulation times. Table 5 shows the numerical L_2 errors of the conserved quantities computed. As expected, the approximate order of convergence is 2.0.

6.5. Sod's shock tube

Sod's shock tube problem, see e.g., [24], is perhaps the simplest and most widely used example to test any numerical method intended for shock hydrodynamics. Its analytical solution is known by solving a 1D Riemann problem. The wave structure consists of a shock moving to the right, a contact discontinuity moving to the right, and a rarefaction wave moving to the left. This is not a severe test but can quickly identify problems with conservation and the wave structure. The flow here is modeled as a 3D tube with a circular cross section of unit length with a diameter of 0.05, with $\gamma = 1.4$, and the following initial conditions:

$$
\begin{aligned}
u_i(x_i) &= 0.0 \\
\rho(x_i) &= \begin{cases} 1.0 & x < 0.5 \\ 0.125 & x \geq 0.5 \end{cases} \\
p(x_i) &= \begin{cases} 1.0 & x < 0.5 \\ 0.1 & x \geq 0.5 \end{cases}
\end{aligned}
\tag{37}
$$

where x is the distance along the length of the tube. The density field is plotted on the surface of Mesh 1 at $t = 0$, and at $t = 0.2$ in Fig. 10. The numerical solution was also extracted at $t = 0.2$ along a line through the center of the tube. The density, velocity, total energy, and pressure are depicted in Fig. 11 for the successively finer meshes given in Table 6 together with the analytical solution.

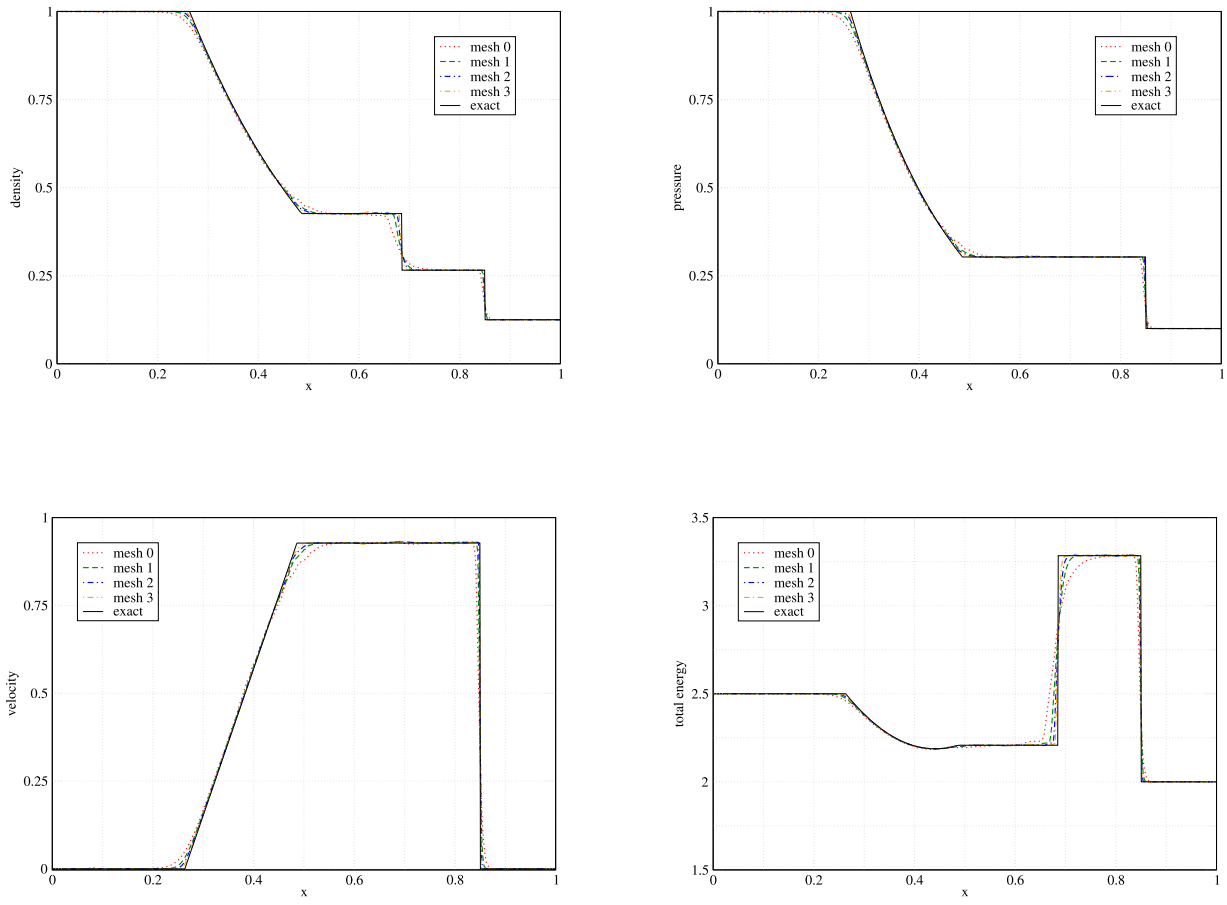

Fig. 11. Density, velocity, pressure, and total energy with their exact solutions along the center of the tube for Sod shock tube problem for 4 different meshes.

Table 6
Mesh sizes for the Sod shock tube problem. Here dx is the average edge length along the length of tube.

Mesh	Points	Tetrahedra	dx
0	7294	34,181	0.840
1	51,794	273,448	0.414
2	389,139	2,187,584	0.206
3	3,014,277	17,500,672	0.103

6.6. Sedov's blast wave

Another test problem with a discontinuous solution is the Sedov problem [27], where a source of energy is defined to produce a shock in a single computational cell at $t = 0$. The Sedov problem is also widely used for shock hydrodynamics. Its solution is a spherically spreading wave starting from a single point and used for testing the ability of numerical methods to maintain spherical symmetry and to resolve sharp gradients. We used three successively finer meshes, given in Table 7, to compute the numerical solution in 3D with $\gamma = 5/3$ and the following initial conditions:

$$\begin{aligned} u_i(x_i) &= 0.0 \\ \rho(x_i) &= 1.0 \\ e(x_i) &= \begin{cases} 1.0 \times 10^{-4} & x_i \neq 0.0 \\ e_s & x_i = 0.0 \end{cases} \end{aligned} \tag{38}$$

where e_s and p_s are mesh-dependent source values summarized in Table 7 along with the corresponding volume V_s of the source region. Note that energy is in units of Mbar $-$ cm^3/g, pressure is in units of Mbar, and source volume is in units of cm^3. These initial conditions correspond to pressure ratios of $\mathscr{O}(10^8)$–$\mathscr{O}(10^{10})$ across a single element.

The numerical solution for the pressure and density at two different instants in time are given in Fig. 12. The numerical solution for the density was also extracted along a line through the x axis using the three meshes. This is plotted in Fig. 13 together with a semi-exact solution at $t = 1.0$ μs.

Table 7
Mesh sizes and source parameters for the Sedov problem. Here h is the average edge length.

Mesh	Points	Tetrahedra	h	V_s	e_s	p_s
1	65,958	362,363	0.029	1.14×10^{-6}	5.42×10^{4}	3.63×10^{4}
2	505,724	2,898,904	0.014	1.78×10^{-7}	3.46×10^{5}	2.32×10^{5}
3	3,956,135	23,191,232	0.007	2.23×10^{-8}	2.77×10^{6}	1.85×10^{6}
4	31,286,637	185,529,856	0.0035	2.79×10^{-9}	2.21×10^{7}	1.48×10^{7}

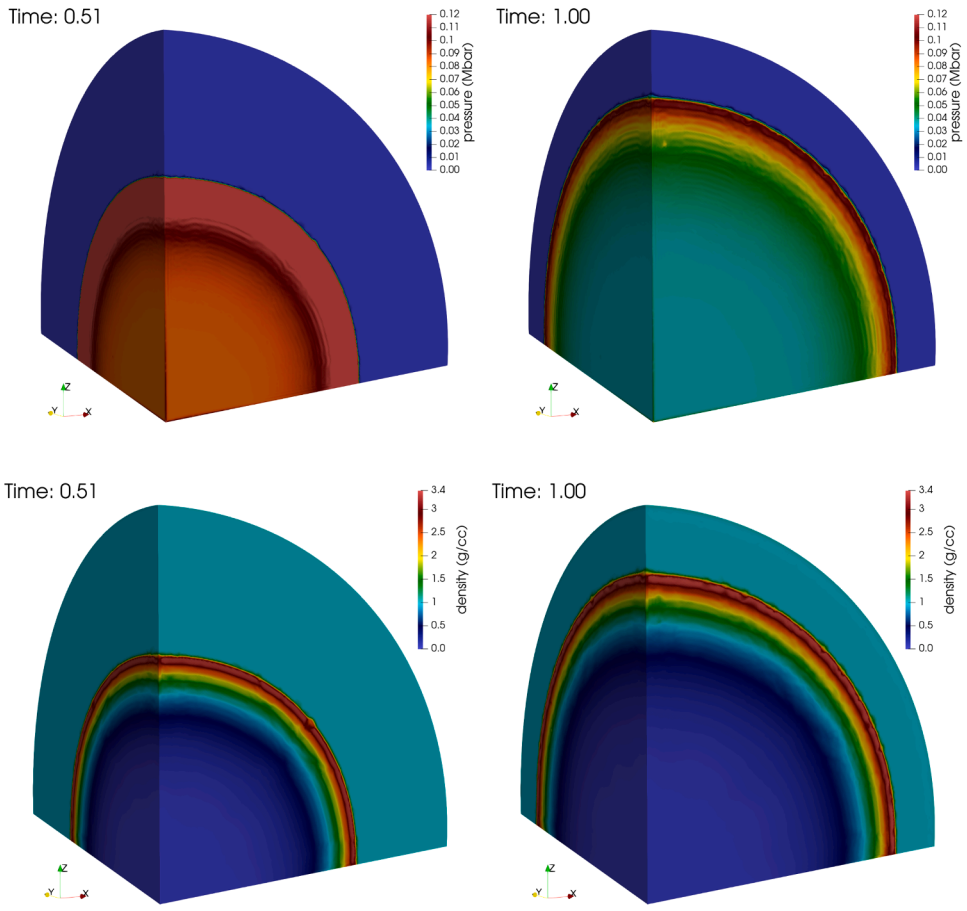

Fig. 12. Surface pressure (top) and density (bottom) for the Sedov problem at $t=0.5\mu s$ and $t=1.0\mu s$ on Mesh 3.

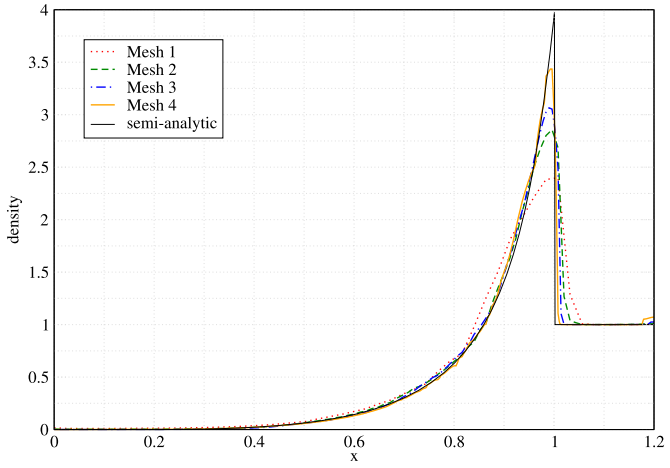

Fig. 13. Density profiles for the Sedov problem with increasing mesh resolution at $t=1.0\mu s$.

7. Parallel performance

This section discusses parallel performance, including strong and weak scaling, the profile of a time step, and we demonstrate automatic load balancing using various strategies available in Charm++.

7.1. Strong scaling

Using increasing number of compute cores with the same problem measures strong scaling, characteristic of the algorithm and its parallel implementation. Strong scalability helps answer questions, such as *How much faster can one obtain a given result (at a given level of numerical error) if larger computational resources were available*. To measure strong scaling we ran the vortical flow problem using a 794 M-cell mesh on varying number of PEs for 100 time steps and measured the wall-clock time for the 100 steps.

Fig. 14 depicts wall-clock times of 100 time steps using a 794 M-cell mesh. The figure shows that strong scaling is close to ideal up to approximately 30 K cores after which communication overwhelms computation. This is an important data point: the recommended minimum load per core for this algorithm on this machine, is about 28 K elements per PE; throwing more resources at this size problem is not economical and, conversely, using less than about 28 K elements per core will likely yield suboptimal performance.

Fig. 14 also shows the difference in performance of the algorithm between Charm++'s SMP (symmetric multi-processing) and non-SMP mode. SMP, compared to non-SMP, mode refers to a number of Charm++ implementation details that allow the runtime system to treat a *logical* compute node as a shared-memory machine, which then allows various optimizations, such as pointer passing instead of communication if both the sender and receiver reside on the same compute node. SMP mode also allows configuring the runtime system to use a designated

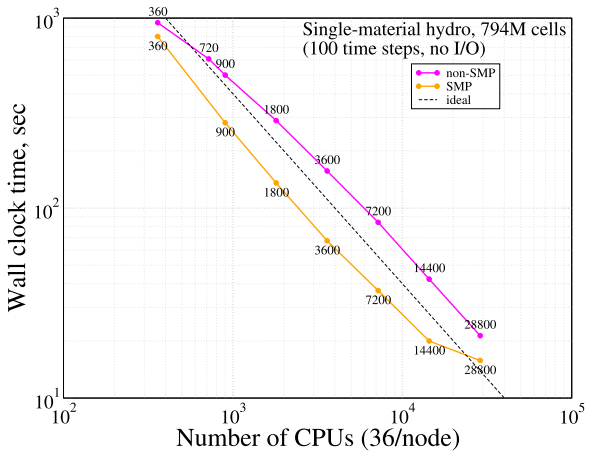

Fig. 14. Strong scaling at $\mathcal{O}(10^4)$ compute cores of the using two different modes of Charm++: non-SMP and SMP.

Table 8
Wall-clock times for time stepping only (measuring 100 time steps) and total time (including mesh load and setup) in Charm++'s non-SMP and SMP modes. The time stepping times are plotted in Fig. 14.

Number of PEs	100 time steps, sec, non-SMP	Total time, sec, non-SMP	100 time steps, sec, SMP	Total time, sec, SMP
360	946	1235	800	2336
720	610	849	375	1345
900	501	723	281	964
1800	289	480	136	578
3600	157	370	67	311
7200	84	312	37	275
14,400	42	408	20	175
28,800	21	930	16	213

compute core (or cores) for every logical node responsible solely for communication and allowing the rest of the cores to only perform computation. Such freedom in configuration allows tailoring the runtime system specific to the hardware by, e.g., taking into account of caches shared by specific compute cores, and in general, allows a more optimal utilization of the multi-level memory hierarchy with non-uniform access costs at each level that is increasingly found in current supercomputing hardware. Simply put, Charm++'s SMP mode can be thought of as MPI + X, where X stands for some programming paradigm for threading and on-node parallelism, e.g., OpenMP, POSIX Threads, or Kokkos. In contrast, Charm++'s non-SMP mode can be thought of as *"MPI everywhere"*, where every compute core is treated as independent with its own memory space. Note that there are no source code changes, additional code, or duplicate kernels that would be required to utilize Charm++ in SMP vs. non-SMP mode. The code uses a single abstraction for parallel programming and that is Charm++. Selecting SMP or non-SMP mode amounts to *building* Charm++ in SMP or non-SMP mode and building and linking the solver the same way to the desired Charm++ instance as a library.

We ran the same code running the same mesh and problem in both SMP and non-SMP mode and performed the strong scaling study for both. Wall-clock times, measuring time-stepping only, as well as total runtimes are given in Table 8, and the former are also plotted in Fig. 14. For all runs, the non-SMP setup corresponded to using all 36 cores of a compute node uniformly, while in SMP mode we designated a core for communication per each of the 2 sockets (18 cores) of a compute node. (This means that in SMP mode, of a total of 14,400 cores, 400 compute nodes, only 13600 were used for actual computation.) Fig. 14 shows that, in general, SMP mode is approximately 2x faster than non-SMP mode, c.f., the corresponding middle columns in Table 8. This is due to the benefits of SMP mode described above.

Table 8 also shows the wall-clock measurements of the total runtimes. It is apparent that at the lower core counts (360–3600) non-SMP mode outperforms SMP mode when measured by total runtime. This is the effect of the unequal performance of reading the mesh followed by mesh data redistribution and the computation of mesh node communication maps in SMP and non-SMP modes. Both modes perform these tasks in parallel, but SMP mode uses 2 parallel streams per compute node, while non-SMP mode uses 36. Thus non-SMP mode will perform better, at lower core counts. The data in the tables also show that this performance figure turns around between 3600 and 7200 PEs, where both SMP and non-SMP mode yield approximately equal total runtimes. At larger core counts (≈ 5 K) and beyond, SMP mode clearly outperforms non-SMP mode. This is expected, considering the limited parallelism of the underlying parallel file system. As expected, at larger

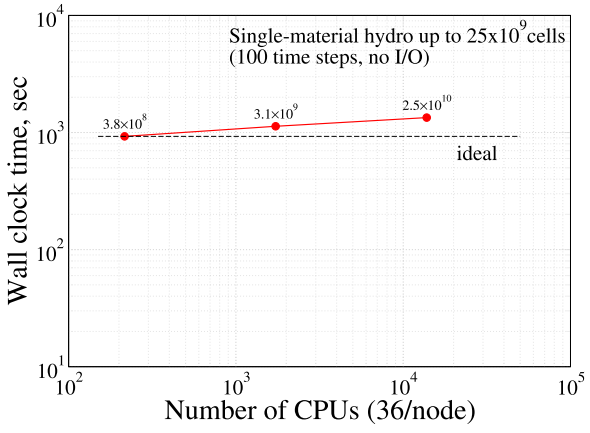

Fig. 15. Weak scaling up to 25 billion cells.

core counts it is more beneficial to use SMP mode, e.g., at 36 K cores, the total runtime of non-SMP mode is almost 6 times that of SMP mode.

7.2. Weak scaling

Fig. 15 depicts wall-clock times of 100 time steps keeping the load per compute node the same. We start with a 48 M-cell mesh and perform an initial uniform mesh refinement before time stepping that replaces every tetrahedron in the computational mesh with 8 smaller ones and thus yields exactly 384 M cells and run this on 6 computes nodes. The next points were obtained by doing two and three refinement steps, respectively, yielding over 3B and almost 25B cells, respectively. Increasing the problem size in exact proportion with the computational resources establishes weak scalability, characteristic of the algorithm and its implementation. Weak scaling enables answering questions, such as *How effective can one use the available (largest) compute resources if ever decreasing numerical errors, e.g., larger resolutions, are required.* Fig. 15 shows that the weak scaling of the algorithm is not ideal: there is an approximate 14% increase of computational cost compared to ideal weak scaling. This quantifies the "cost" of the algorithm and its implementation when used at ever larger scales (both larger problems and larger compute resources).

7.3. Computational cost profile

Fig. 16 depicts the relative CPU utilization of the various computational tasks during 100 time steps in SMP mode. This run was done on 25 physical compute nodes, using 2 logical nodes per compute node, designating 2 PEs per each compute node for communication only, which leaves 850 worker PEs. The figure shows that the right hand side computation (gather+scatter) takes about 40% of a time step: this step consists of both tasks `RHS` and `DIF`, computing the right hand side of Eq. (1) including the flux and source terms for both the low and high order solutions (including mass diffusion). Another significant portion, 30%, is `aec` + `alw`, computing the anti-diffusive element contributions and the minimum and maximum increments of allowed solution values in mesh nodes, respectively, prerequisites of the FCT limiting procedure. Computing the limit coefficients, task `lim` computing Eqs. (21)–(24) in each node, costs a little over 10%. About 2–5% of the cost, purple in Fig. 16, is the cost of computing the size of the next time step size. The figure also shows that 10–15% of the total runtime is spent idle, when CPUs are waiting for messages without doing any useful work. Finally, the tiny black gaps between the white `idle` and the top of the figure denoting 100% is the cost of the runtime system: scheduling, sending and receiving messages, etc.

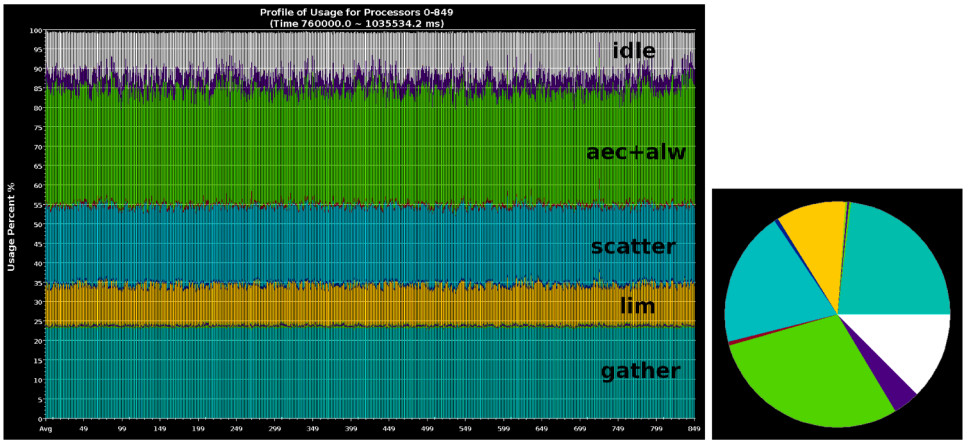

Fig. 16. Average relative CPU utilization across 100 time steps and 850 worker CPUs. On the pie chart, communication cost: red – rhs communication: 0.7%, between yellow and light blue, green + blue + green – `comaec` + `comalw` + `comlim`: 1.2%. (For interpretation of the references to color in this figure legend, the reader is referred to the web version of this article.)

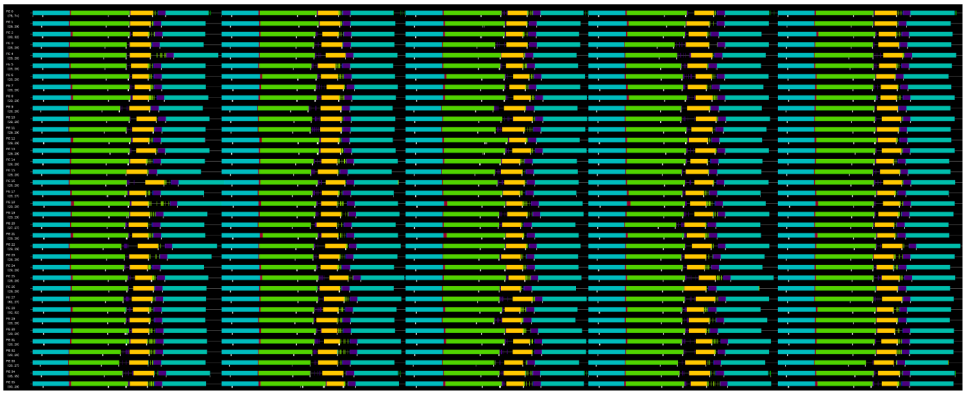

Fig. 17. CPU utilization across 5 time steps on a single compute node (36PEs) from a 900-core run on 25 compute nodes. The task coloring corresponds to that of Fig. 16 and the small white vertical lines denote message sends. Note that the right hand side calculation, see Eq. (9), is broken up into two parts, since the gather step can be computed before the new Δt is available, followed by the scatter step, allowing overlap of computation and communication.

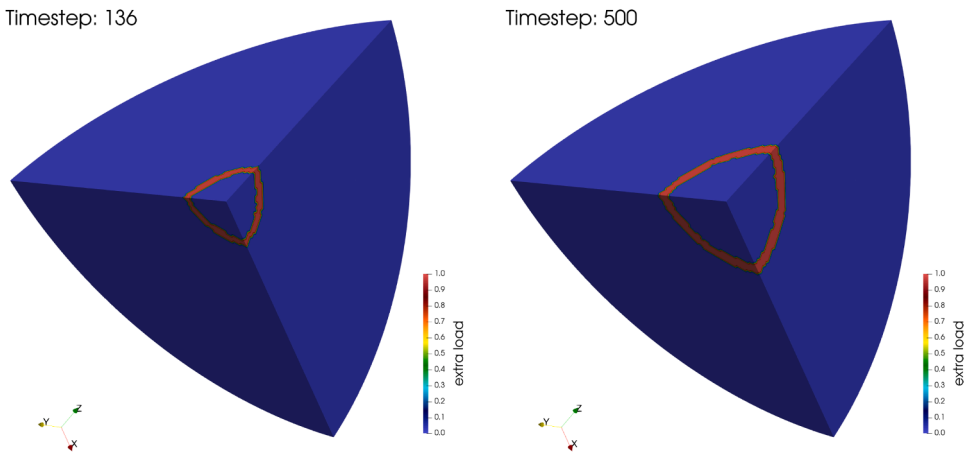

Fig. 18. Spatial distributions of the extra load, corresponding to the fluid density exceeding the value 1.5, during the time evolution of the Sedov problem on the 300k-cell mesh: (left) shortly after the onset of load imbalance, (right) at end of the simulation.

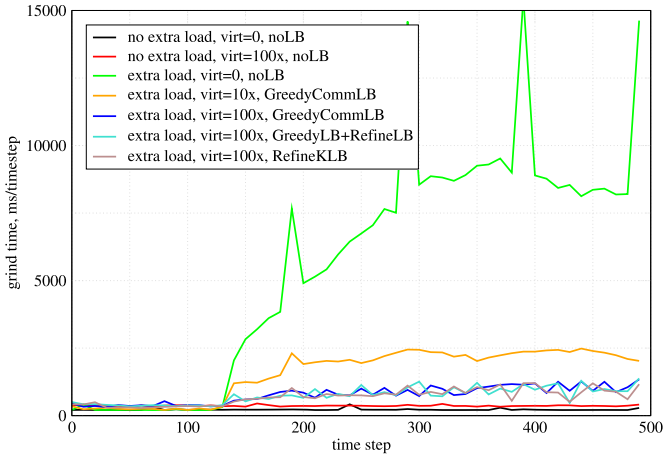

Fig. 19. Grind-time during time stepping computing a Sedov problem without and with extra load in cells whose fluid density exceeds 1.5, inducing load imbalance, without and with load balancing. These simulations were run on a shared-memory workstation, in SMP mode, using 30 worker threads + 2 communication threads, on a 300K-cell mesh. Load balancing was invoked at every 10th time step for all load balancers.

Table 9
Timings for the Sedov problem, using a 300K-cell mesh, without and with extra load without and with load balancing on a shared-memory machine.

Case	Extra load	Virtualization	Charm+ load balancer	Median grind-time, ms/step	Total time, s	Speedup relative to case 3
1	no	—	—	215	93	—
2	no	100 ×	—	362	148	—
3	yes	—	—	6898	2567	1.0 ×
4	yes	10 ×	GreedyCommLB	2027	656	3.9 ×
5	yes	100 ×	GreedyCommLB	788	312	8.2 ×
6	yes	100 ×	GreedyLB+RefineLB	752	315	8.1 ×
7	yes	100 ×	RefineKLB	732	310	8.2 ×

The pie-chart in Fig. 16, helps appreciate the communication costs. On the pie-chart, the tiny dark red section on the left depicts the cost of the communication (0.7% of a time step) of the right hand side (the rhs and diffusion). The cost of communication tasks, `comaec`, `comalw`, and `comlim`, see also Fig. 3, are depicted as almost vertical sections on the right between the light blue `gather` and the yellow `lim` slices. Their combined cost is 0.38% + 0.44% + 0.36% ≈ 1.2%. This puts the total relative cost of communication to just below 2% of the total runtime of time stepping. The dark blue section between the yellow `lim` and other light blue `scatter` (0.7%) depicts the total cost of combining the own and communicated portions of the limited AECs, Eq. (24), and of applying the limited solution, Eq. (25).

Fig. 17 gives an idea of the CPU utilization by the different tasks in time and their overlapped execution due to asynchrony. The figure depicts 5 consecutive time steps on a single compute node, displaying 36 PEs on the vertical axis. Based on the minimum, maximum, and average number of elements across the 850 mesh partitions, respectively, 934,152, 934,153, and 934,152, one would think that CPU utilization should be very well-balanced. However, the timeline shows that even this extremely homogeneous load distribution results in appreciable idle times at the end of time steps, denoted by black between the blue gather and scatter regions. This adds up to the 10–15% average idle time, discussed above. This is likely caused by the uneven load due to the unequal number of boundary points among chares: mesh partitions in a

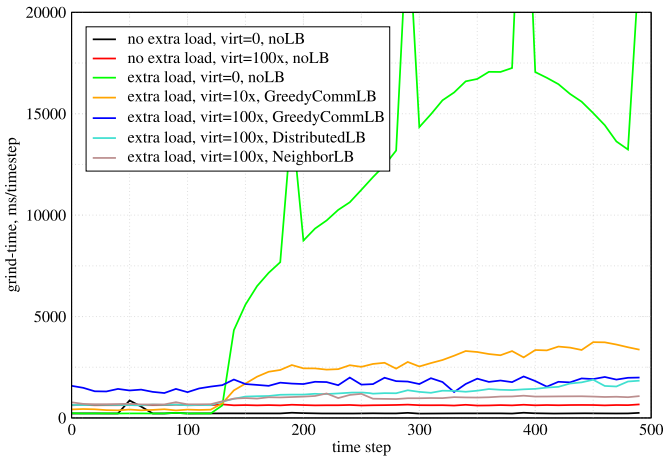

Fig. 20. Grind-time during time stepping computing a Sedov problem with extra load in cells whose fluid density exceeds the threshold of 1.5, inducing load imbalance. These simulations were run on a distributed-memory cluster on 10 compute nodes, in SMP mode, using 34 worker threads + 2 communication threads per node, on a 3M-cell mesh. Load balancing was invoked at every 10th time step for all load balancers.

corner of the cube have many boundary points compared to internal mesh partitions without any boundary points. As a result, computation work will inevitably differ on different PEs.

While improvements to the above CPU utilization (e.g., to reduce the idle time and increase overlap) are likely possible, there are three important conclusions we can draw from the above discussion:

1. The overhead of the runtime system is negligible compared to useful computation and communication.
2. The communication costs (≈ 2%) are acceptable, especially considering the higher level (and safer) abstraction allowed by Charm++ compared to MPI-style programming, see also Listing 1.
3. Even well-balanced distributed problems (measured by the number of computational cells) may lead to appreciable idle times.

7.4. Load balancing

To exercise the built-in load balancers in Charm++, and to demonstrate them for an unstructured-grid solver, we have computed the Sedov problem, adding some extra computational load to those cells whose density exceeds the value of 1.5. This mimics, e.g., combustion (e.g., a burn front), non-trivial material equations of state, etc., and represents realistic load imbalance, characteristic of multi-physics simulations.

Fig. 19 depicts the simulation time during time stepping, measured in ms/step, for a number of shared-memory runs on a 300K-cell mesh (mesh 1), taking 500 time steps. One can see that the density peak exceeds the value of 1.5 around the 130th time step, inducing load imbalance and this persists until the end of the simulation. The extra load corresponds to the cells depicted in Fig. 18, displayed at two different times. It is clear from Fig. 19 that multiple load balancing strategies can successfully and effectively homogenize the uneven, dynamically generated, a priori unknown computational load. The common requirement for effective load balancing is fine-grained work units, ensured by increasing the degree of overdecomposition (virtualization) from 1 to 100x, which yields 100× the mesh partitions compared to the number of CPUs the problem is running on. As expected, increasing the number of partitions beyond the number of CPUs has a cost due to increased communication cost, c.f., black and red lines. Table 9 shows some timings without and with load balancing. For this setup the GreedyCommLB load balancer performs the best, yielding 8.2x speedup compared to using no load balancing.

Fig. 20 shows simulation times for a larger, 3M-cell mesh (mesh 2), run on 10 computes nodes of a distributed-memory cluster with 36 CPUs/node. Except the larger mesh run on a cluster, everything else is the same as before. For the distributed-memory computations, besides centralized load balancers (GreedyCommLB, GreedyRefineLB, RefineLB, RefineKLB), here we have also used distributed load balancers, e.g., DistributedLB and NeighborLB, available in Charm++. As their name suggests, centralized load balancers collect load imbalance information to a single PE, but their decision is more accurate due to full knowledge of the entire simulation on a single PE. On the other hand, distributed load balancers only exchange neighbor information thus they are less accurate but cost less. This is consistent with our findings in Fig. 20 as well as the timings in Table 10. For this problem, the best performance is achieved by NeighborLB with a speedup over 10× compared to no load balancing.

As shown, excellent performance can be obtained on both shared-, and distributed-memory machines using the built-in automatic load balancers of Charm++. We emphasize that we wrote no load balancing code: we simply ensure overdecomposition and turn on load balancing; the runtime system measures real-time CPU load and automatically performs object migration to homogenize the load. This is particularly beneficial for applications with *a priori* unknown or dynamically

Table 10
Timings for the Sedov problem, using a 3M-cell mesh, with extra load with and without load balancing on 10 compute nodes of a distributed-memory cluster.

Case	Extra load	Virtualization	Charm+ load balancer	Median grind-time, ms/step	Total time, s	Speedup relative to case 3
1	no	—	—	222	93	—
2	no	100 ×	—	630	359	—
3	yes	—	—	11,562	4618	1.0 ×
4	yes	10 ×	GreedyCommLB	2530	1231	3.8 ×
5	yes	100 ×	GreedyCommLB	1685	1058	4.4 ×
6	yes	100 ×	DistributedLB	1209	514	9.0 ×
7	yes	100 ×	NeighborLB	995	430	10.7 ×

changing load distribution, ubiquitous in multiphysics simulations and characteristic of heterogeneous performance of large data centers. The data also demonstrates that the cost of load balancing is negligible compared to the savings over the unbalanced problem without load balancing.

8. Summary and conclusions

This paper discussed the implementation, verification, and parallel performance of a node-centered continuous Galerkin finite element flux-corrected transport algorithm for the simulation of high-speed compressible fluid dynamics on large 3D unstructured meshes using the Charm++ tasking runtime system. We have also demonstrated the benefits of automatic load balancing in Charm++ with irregular workloads.

The source code with documentation is available at https://quinoacomputing.org. Using the Charm++ runtime system enables automatic overlap of computation, communication, and I/O, and therefore good scalability, and allows automatic load balancing, i.e., *without* requiring any code from the application developer, and independent of the source of the load imbalance, e.g., higher temperatures at a corner of the data center, a slower CPU or adaptive mesh refinement, to name a few. Load balancing can simply be enabled and computational load is homogenized, using continuous real-time CPU load measurement by the runtime system, using advanced strategies, across large distributed-memory computations. The main price for these features, in our opinion, is a somewhat steep learning curve of the asynchronous programming paradigm, which yields a highly nonlinear software structure and a new family of (asynchronous, i.e., non-deterministic) problems during code development.

CRediT authorship contribution statement

J. Bakosi: Conceptualization, Software, Validation, Writing - review & editing, Supervision, Funding acquisition, Project administration. **R. Bird:** Software, Validation. **F. Gonzalez:** Software, Validation. **C. Junghans:** Software, Funding acquisition, Project administration. **W. Li:** Software, Validation. **H. Luo:** Software, Validation. **A. Pandare:** Software, Validation. **J. Waltz:** Software, Validation.

Declaration of Competing Interest

The authors declare that they have no known competing financial interests or personal relationships that could have appeared to influence the work reported in this paper.

Acknowledgments

The first author thanks Charmworks, Inc., for their helpful suggestions regarding load balancing, their Projections tool, and programming with Charm++ in general. The first author also thanks Neil Carlson of Los Alamos National Laboratory for suggesting the algorithm used for computing the nodal communication maps in parallel, for many discussions on solving partial differential equations on unstructured meshes, and software development in general. The work presented in this paper was supported by the Laboratory Directed Research and Development program of Los Alamos National Laboratory under project number LDRD-20170127-ER. LANL Report LA-UR-20-21450.

Supplementary material

Supplementary material associated with this article can be found, in the online version, at doi:10.1016/j.advengsoft.2020.102962

References

[1] Hirsch C. Numerical computation of internal and external flows1. The MIT Press; 1988.
[2] LeVeque R. Finite volume methods for hyperbolic problems. Cambridge texts in applied mathematics. Cambridge University Press; 2002, ISBN 9781139434188. https://books.google.com/books?id=mfAfAwAAQBAJ.
[3] Löhner R. Applied computational fluid dynamics techniques: an introduction based on finite element methods. Wiley; 2008.ISBN 9780470519073, https://onlinelibrary.wiley.com/doi/book/10.1002/9780470989746
[4] Löhner R, Morgan K, Peraire J, Vahdati M. Finite element flux-corrected transport (FEM-FCT) for the Euler and Navier–Stokes equations. Int J Numer Meth Fluids 1987;7(10):1093–109. https://doi.org/10.1002/fld.1650071007.
[5] Lax P, Wendroff B. Systems of conservation laws. Commun Pure Appl Math 1960; 13(2):217–37. https://doi.org/10.1002/cpa.3160130205.https://onlinelibrary.wiley.com/doi/abs/10.1002/cpa.3160130205
[6] Donea J. A Taylor–Galerkin method for convective transport problems. Int J Numer Meth Eng 1984;20:101–11.
[7] Löhner R, Morgan K, Zienkiewicz OC. The solution of non-linear hyperbolic equation systems by the finite element method. Int J Numer Methods Fluids 1984;4 (11):1043–63. https://doi.org/10.1002/fld.1650041105.https://onlinelibrary.wiley.com/doi/abs/10.1002/fld.1650041105
[8] Godunov SK. Eine Differenzenmethode für die Näherungsberechnung unstetiger Lösungen der hydrodynamischen Gleichungen. Mat Sb Nov Ser 1959;47:271–306.
[9] The design of flux-corrected transport (FCT) algorithms for structured grids. In: Kuzmin D, Löhner R, Turek S, editors. Berlin, Heidelberg: Springer Berlin Heidelberg; 2005. p. 29–78.ISBN 978-3-540-27206-9
[10] *Charm++:* Parallel programming framework; http://charmplusplus.org.
[11] *Charm++:* Parallel programming framework research; http://charm.cs.illinois.edu/research/charm.
[12] Kale LV, Krishnan S. Charm++: a portable concurrent object oriented system based on c++. SIGPLAN Not 1993;28(10):91–108. https://doi.org/10.1145/167962.165874.
[13] Shu W, Kale L. Chare kernel—A runtime support system for parallel computations. J Parallel Distrib Comput 1991;11(3):198–211. https://doi.org/10.1016/0743-7315(91)90044-A.
[14] Kale L, Bhatele A. Parallel science and engineering applications: the charm++ Approach. Series in Computational Physics. CRC Press; 2016.ISBN 9781466504134, https://books.google.com/books?id=xbzMBQAAQBAJ
[15] *Zoltan: Parallel Partitioning and Load Balancing*; http://www.cs.sandia.gov/Zoltan.
[16] *ExodusII:* The Sandia Engineering Analysis Code Access System (SEACAS) is a suite of preprocessing, postprocessing, translation, and utility applications supporting finite element analysis software using the Exodus database file format; https://github.com/gsjaardema/seacas.
[17] Kidder LE, Field SE, Foucart F, Schnetter E, Teukolsky SA, Bohn A, et al. SpECTRE: A task-based discontinuous Galerkin code for relativistic astrophysics. J Comput Phys 2017;335:84–114. https://doi.org/10.1016/j.jcp.2016.12.059.http://www.sciencedirect.com/science/article/pii/S0021999117300098
[18] Waltz J. Derived data structure algorithms for unstructured finite element meshes. Int J Numer Meth Eng 2002;54(7):945–63. https://doi.org/10.1002/nme.453.
[19] Li W, Luo H, Bakosi J. A *p*-adaptive discontinuous Galerkin method for compressible flows using Charm++. AIAA scitech 2020 forum, Orlando, Florida, 6–10 January, 2020. 2020.
[20] Waltz J, Canfield T, Morgan N, Risinger L, Wohlbier J. Verification of a three-dimensional unstructured finite element method using analytic and manufactured solutions. Comput Fluids 2013;81:57–67. https://doi.org/10.1016/j.compfluid.2013.03.025.http://www.sciencedirect.com/science/article/pii/S0045793013001333
[21] Waltz J, Canfield T, Morgan N, Risinger L, Wohlbier J. Manufactured solutions for the three-dimensional Euler equations with relevance to inertial confinement fusion. J Comput Phys 2014;267:196–209. https://doi.org/10.1016/j.jcp.2014.02.040.http://www.sciencedirect.com/science/article/pii/S0021999114001661
[22] Boffetta G, Mazzino A. Incompressible Rayleigh-Taylor turbulence. Annu Rev Fluid Mech 2017;49(1):119–43. https://doi.org/10.1146/annurev-fluid-010816-060111.https://doi.org/10.1146/annurev-fluid-010816-060111
[23] Livescu D, Ristorcelli J, Gore R, Dean S, Cabot W, Cook A. High-Reynolds number Rayleigh–Taylor turbulence. J Turbul 2009;10(13). https://www.tandfonline.com/doi/full/10.1080/14685240902870448.
[24] Kamm J, Brock J, Brandon S, Cotrell D, Johnson B, Knupp P, et al. Enhanced verification test suite for physics simulation codes. Tech. Rep. Los Alamos National Laboratory; 2008.
[25] Waltz J. Microfluidics simulation using adaptive unstructured grids. International Journal for Numerical Methods in Fluids 2004;64(9):939–60. https://doi.org/10.1002/fld.753.
[26] Taylor GI, Green AE. Mechanism of the production of small eddies from large ones. Proc R Soc Lond Ser A- Mathematical and Physical Sciences 1937;158(895): 499–521. https://doi.org/10.1098/rspa.1937.0036.
[27] Sedov L. Similarity and dimensional methods in mechanics. Taylor & Francis; 1993.ISBN 9780849393082; https://www.books.google.com/books?id=xXSg388Su38C